Analysis and Design of MHz-range Wireless Power Transfer Systems for Implantable Devices

Luis Carlos Gutiérrez Lázaro

Delft 2013

Biomedical Electronics Laboratory, EEMCS
Delft University of Technology
Mekelweg 4, 2628 CD Delft, The Netherlands
Phone +31 (0) 152784568
info@tudelft.nl
ewi.tudelft.nl

Analysis and Design of MHz-range Wireless Power Transfer Systems for Implantable Devices

Luis Carlos Gutiérrez Lázaro

A Thesis Submitted to
The Faculty of Electrical Engineering, Mathematics and Computer Science in Partial Fullfillment of the Requirements for the Degree of
MASTER OF SCIENCE
in Electrical Engineering

Supervisor: Dr. ir. Wouter A. Serdijn

Thesis committee

Dr. ir. Wouter A. Serdijn
Dr. ir. Chris Verhoeven
Dr. ir Rob Remis
Ir. Mark Stoopman

Delft University of Technology

November 2013

Dedicated to my beloved parents

Summary

Wearable and implantable devices are becoming more and more common as time goes by and one of the major bottlenecks in their development is the power delivery. In order to tackle this problem, energy harvesting arises an option to bring these devices one step closer to complete autonomy. Among the available mechanisms for harvesting, near-field inductive coupling appears as a good alternative due to the flexibility it offers in terms of size and output power. Although a certain level of maturity has been reached over the last decade, a sort of mysticism still exists around the wireless power transfer. To the author's best knowledge, none of the works found in literature addresses the entirety of the problem. Here, a comprehensive, generalized analysis and design are made starting from the from the very differentiation of the near and far-field regimes all the down to circuit design.

Studying the inductively coupled interfaces allow us to estimate the performance of the link prior to any design attempt, serving as a very useful tool in the feasibility evaluation of certain application. In particular, models for the coupling factor and losses of the magnetic link are introduced. Emphasis is made on comparing the performance of the links in a resonant and non-resonant regime.

An implantable device for neural stimulation/recording with a rechargeable Li-Ion as an energy storage is considered as our intended application. This requires us to realize an study of the impact of tissue in energy transfer and viceversa. From here, the circuit design of a wireless power transfer interface is presented. All circuit blocks necessary for transfer are designed and simulated, allowing us to have a complete overview of the system.

Preface

The present work is the result of more than a year of work, liters of coffee, simulation crashes and sleepless nights. However, it has also been a great challenge with a lot of high notes and eureka moments. I hope this work contributes (at least in a small portion) to the development of biomedical devices, in particular energy harvesting and wireless power transfer.

Happy reading,

Delft, November 22, 2013

Luis Carlos Gutiérrez Lázaro

Acknowledgements

The work you have in your hands right now (or more likely in the screen of your computer) would have not been possible without the help of many people surrounding me. First of all, I would like to thank my supervisor, Prof. Wouter Serdijn for giving me the opportunity of being part of his research group and all his coaching throughout the development of this work. He is a person who I admire and from who I have learned a lot. Thanks for "hiring" me as the bass player of the ELCA band and the photographer of BioCAS. I would also like to thank to Mark Stoopman for always being willing to help me solve any problems that I have had, from circuit design and simulations to translation of correspondence in dutch.

None of this would have been possible without the helping hand, love and support of my family, especially my parents. Thanks for keep believing in me in the goods and the bads, the highs and the lows. No need to worry anymore... I'm graduating !

My entire experience in Delft would have not been half as good without "a little help from my friends". Thanks to all of you who I shared a moment with, a beer or a discussion about the weather. I will certainly miss you all.

Thanks to COLFUTURO for making this trip to the Netherlands possible, allowing me to achieve one of my greatest goals in life.

Finally, a very special *dziekuje bardzo* to *moja kochana* Marysia. *Przepraszam* for not learning polish in this 3 and a half years... *ale kocham cie doida !*

Contents

List of Figures

List of Tables

Chapter 1

Introduction

In a world full of engineering marvels and technological advancements, it is undeniable that, to a large extent, the electronics field has played a major role in shaping society by changing consumption patterns, modifying life styles and even the way people interact and take care of themselves. Particularly, the field that benefited the most from this situation is medical science. Countless devices ranging from diagnostic to therapeutic and investigative have arisen thanks to the fast and steady growth of microelectronics.

Over the course of time, better performance and lower power consumption combined with size reduction made it possible to develop implantable devices such as pacemakers, cochlear implants, and neurorecorders/stimulators. In recent years, further evolution of ultra low-power integrated circuits and communications has enabled engineers to take wireless sensors and actuators to a complete new level, giving birth to the so called Wireless Body Area Networks WBAN.

The concept of WBAN appeared in the mid 90's from the idea of using wireless personal area networks to communicate with the devices within, on, and in the immediate surroundings of the human body [1]. The possibilities are virtually endless: This technology would allow, for instance, healthcare services at the home of the patient, by remotely monitoring relevant signals coming from their implanted and wearable sensors. Many experts agree that in the coming

decades this market will mature significantly, expanding the usage of such devices beyond the scope of illness treatment to also detect diseases at very early stages, improving quality of life [2, 3]. However, in order to turn this vision into a reality, several challenging factors need to be tackled. Among them, device autonomy appears to be the biggest hurdle.

Although battery technology has evolved significantly in the last years, they have not kept pace with other developing technologies related to mobile electronics [4]. Figure 1.1 represents the performance increase in laptop computers, showing that batteries have had the slowest evolution in mobile electronics [5]. Moreover, size constraints limit their performance and due to their electrochemical nature they degrade over time until becoming completely unusable. In addition, they pose a problem on replacement and disposal, particularly critical when referring to implants. Fortunately, power constraints can be relaxed by energy harvesters or energy scavengers. By doing this, in essence it could be possible to reach a point where durability is no longer limited by an adjunct energy store but by the device's physical survival itself. Considering that Energy Harvesting (EH) is still in its early stages, there is ample margin for further study and improvement. This research focuses on energy scavenging, targeted for implantable devices.

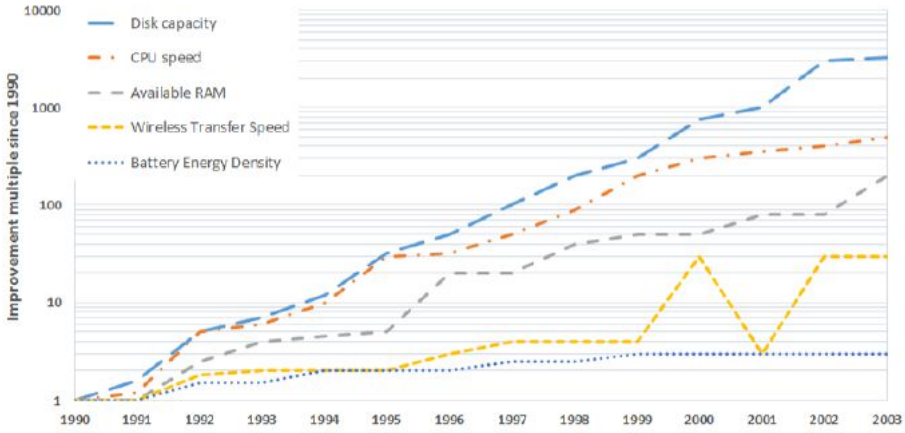

Figure 1.1: Improvement of mobile technologies since 1990. Courtesy of [5].

1.1 Energy Harvesting

Throughout history, people in The Netherlands have had to strive to keep their feet dry. A lot of effort and innovation was required to withstand the force of the sea to prevent flooding. Without a doubt, windmills and watermills are a dutch trademark and a symbol of the Netherland's constant struggle to keep water out. From a broader perspective, however, these machines can also be considered as large energy scavengers. They use energy available in the environment to perform a task, being water pumping, grain grinding or any

other kind of activity. Wind turbines, solar collectors and tidal generators are examples of environmental energy capturing. However, the energy obtained from these processes (e.g. rotational movement, heat capture) do not need to be used directly; it can also be converted into electricity to provide power at a distant location or to be stored in batteries for latter use. Whilst the primary goal of large scale harvesting is to cut down carbon emissions, small energy scavenging aims mainly towards the possibility of creating autonomous devices. Many physical phenomena have been studied to obtain harvesters suitable for portable devices, aiming at high efficiencies and minimum size overhead. This section presents a brief overview of the most common existing harvesting techniques.

1.1.1 Optical

Solar cells are perhaps the most popular and mature version of optical harvesters. They are commercially well established and are a proven technology of energy scavenging. The principle of operation involved is the use of electromagnetic radiation via the photovoltaic effect. In general, *the photovoltaic effect* is described as the generation of a potential difference at the junction of two different materials in response to visible light or other radiation [6]. Fig. 1.2 shows the typical structure of a crystalline silicon solar cell.

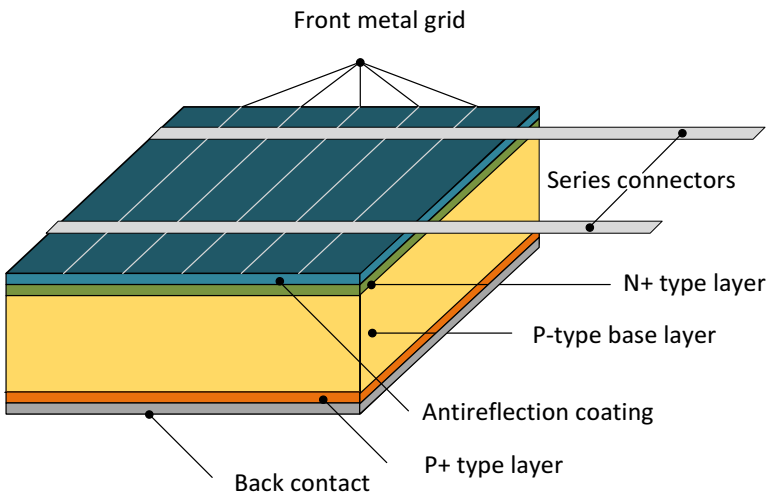

Figure 1.2: Typical c-Si solar cell.

Contrary to solar collectors, in which sunlight is concentrated and captured to boil water that rotates an electric generator, solar panels based on the photovoltaic effect generate electricity directly by creating electron-hole pairs. Roughly speaking, the irradiance from bright sunlight averages at 100 mW/cm^2 whereas it reaches up to 100 $\mu W/cm^2$ under well illuminated indoor conditions [7]. While cost is a key parameter for large-scale photovoltaic generation, at the small scale of portable electronic devices this is less of an issue, and light availability is instead the key limitation [8]. The first handheld appliances that used light as their power source were introduced in the late 70's, when hand calculators and watches powered by embedded photovoltaic panels appeared.

In the biomedical field, some works have succesfully developed protoypes that use the photovoltaic effect to deliver optical power to subcutaneous implanted devices. In [9], the suggested approach is to harvest the energy of light within the therapeutic window[1] by using small size subcutaneous photovoltaic cells. Their results show that the minimum expected loss is 40 dB at λ = 700 nm for a device under the skin and 1 mm fat. Moreover, an extra attenuation of 17 dB should be added per mm when assuming homogenous tissue. A similar approach is presented in [11], where a dedicated near infrared light source at λ = 810 nm with a power density of 22 mW/cm^2 is used to recharge a pacemaker. An implanted photodiode array of 2.1 cm^2 under 0.8 mm of skin in this conditions is sufficient to allow a 20 μA pacemaker to operate for 24 hours. The observed temperature increase is around 1.4 °C, which is considered safe for this kind of tissue [12]. For a 2 mm depth implant, a photodiode array of 10 cm^2 would be necessary in order to maintain the same temperature rise and transmission power.

In both cases, it can be observed that the major constraints in the usage of optical scavenging are the very limited implantation depth and the area requirement at the receiver side. Moreover, the location of the implant is restricted to skin that is continuously exposed, otherwise a dedicated light source must be used and applied directly for a certain amount of time.

1.1.2 Thermoelectric

Temperature differences exist nearly everywhere in both natural and man-made environments. The Thermoelectric Effect (TE) is the direct conversion

[1] The therapeutic window defines the range of wavelengths where light has its maximum depth of penetration in tissue. In the near infrared area, scattering is the most dominant light-tissue interaction, and therefore the propagating light becomes diffused rapidly. Since scattering increases the distance travelled by photons within tissue, the probability of photon absorption also increases [10].

of temperature differences into electric voltage and viceversa. Thomas Johann Seebeck is largely credited for discovering that different metals placed across a temperature gradient could deflect a compass needle. The basic element involved in TE harvesting is the thermocouple (Fig. 1.3(a)). Several thermocouples can be connected electrically in series and thermally in parallel to form a thermopile (Fig. 1.3(b)) in order to generate larger voltages from a particular temperature difference. In a junction of two materials with dissimilar Seebeck coefficients S_A and S_B, the generated voltage can be expressed as in eq. (1.1):

$$V = \int_{T_1}^{T_2} [S_B(T) - S_A(T)]\, dT \tag{1.1}$$

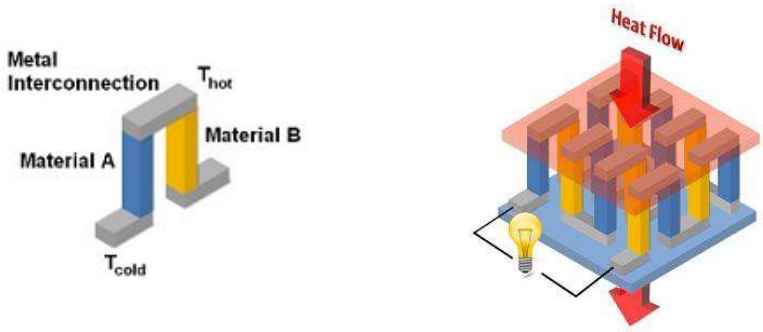

(a) Thermocouple (b) Thermopile

Figure 1.3: Building blocks of a TE harvester. Courtesy of [13].

Semiconductors typically have a high Seebeck coefficient and that is why these materials are commonly used for thermocouples [13]. Furthermore, n-type and p-type semiconductors have Seebeck coefficients with different signs; hence, if the two semiconductors composing a thermocouple have opposite doping, the contributions to the output voltage of eq. (1.1) are summed. Energy conversion, however, limits the functionality of available thermopile arrays, which attain efficiencies well under 10% for 200°C to 40°C, but below 1% for 40°C to 20°C[14].

In the case of human body applications, the thermal gradients that can be obtained are generally very low and thus it is not a straighforward task to obtain voltage levels sufficient to power integrated circuitry. For example, commercial thermopiles commonly use bismuth telluride (Bi_2Te_3) with a Seebeck coefficient S = ± 0.2 mV/°C. By using this material for the thermocouple pillars and a temperature difference of ΔT = 1°C, 5000 thermocouples having a total area of about 25 cm^2 are required to produce a voltage drop ΔV = of 1V [15]. A more realistic approach using the values of thermal resistance for Bi_2Te_3 presented in [13] shows that, in fact, the required area to provide a 1V differential should be 83 cm^2. Table 1.1 shows the calculated thermal gradients in human tissue at different levels of metabolic activity. Here, it is possible to observe that the abdominal area would be the most suitable place to implant a TE harvester; however, in order not to restrain movement, much higher efficiencies should be achieved such that the effective area of the implant can be reduced. In addition, flexible materials could allow larger implants without mobility restrictions.

Table 1.1: Calculated temperature gradients in human tissue [16].

Site	Muscle [mm]	Fat [mm]	Rested ΔT [K]	Walking ΔT [K]	Running ΔT [K]
Abdomen	16	15	1.7	3.8	4.8
Biceps	35	3	0.5	1.2	1.7
Calf-posterior	65	5	0.7	1.7	2.4
Chest	34	7	0.9	2.4	3.2
Forearm	26	3	0.4	1.2	1.6
Hamstring	69	7	0.9	2.3	3.1
Lumbar	37	6	0.9	2.2	3.0
Quadriceps	55	6	0.8	2.1	2.9
Subcapsular	24	8	1.1	2.6	3.4
Suprapatellar	29	6	0.8	2.1	2.8
Triceps	42	6	0.8	2.0	2.8

A TE harvester presented in [17] delivers an output power of 1 μW with an occupied area of 1 cm^2 and a thermal gradient of 5K. ThermoLife [18] developed a commercially available system that provides 30 μW (10 μA at 3V) at a matched load, when the temperature difference is 5K. This device has a volume of 95 mm^3 and weighs 0.23 g.

1.1.3 Kinetic

By definition, a Kinetic Energy Harvester (KEH) is a device that captures energy from any mechanical motion. Researchers developed a backpack with

piezoelectric straps that can deliver over 40 mW of power at a walking pace from a 100 pounds load [19]. In the University of Auckland in New Zealand, an athletic shoe equipped with a lightweight acrylic membrane was designed, which in theory can provide an output power between 30-40 mW using 1 cm^2 of Dielectric Elastometer Generator (DEG) [20]. At this levels, one could store enough energy to power a LED headlamp, a GPS or a phone for a short emergency call. The former devices, however, require heavy loads, high impact activity to perform correctly, which makes them unsuitable for implantable biosensors and stimulators. Depending on the nature of the transducer involved, KEHs can be classified as electromagnetic, electrostatic or piezoelectric. Some of the state-of-the-art concepts addressing in/on body applications are presented below.

1.1.3.1 Electromagnetic

KEH using electromagnetic transducers are able to generate an electromotive force due to the change of an external magnetic flux through a closed circuit [13]. The "Seiko Kinetic" wristwatch uses the wrist motion transmitted by an oscillating weight to a magnetic rotor linked to a coil [21]. In [22], a pacemaker is charged using the same principle, exploiting the heartbeats of a dog. When implanted, this KEH is able to collect 80 mJ after 30 min with a cardiac frequency around 200 beat/min. Two limitations of this approach are the inevitable wear out of the mechanical parts that would make the system require maintenance or replacement after sometime and the size constraint on the oscillating weight for the cases of low-invasive implantable applications.

1.1.3.2 Electrostatic

KEH based on electrostatic transducers use varactors in which the position of their plates is changed by an external force. They may operate in two modes: fixed charge or fixed voltage. Working with a fixed charge, the external force modifies the voltage across the varactor, whereas working with a fixed potential, the motion of the plates generates current through the varactor. Regardless of the operation mode, however, electrostatic KEHs need to be precharged to operate properly. This technique has low efficiency when high power is required, but works quite well with devices having low-power requirements, such as implantable biosensors [13]. A MEMS electrostatic KEH providing 80 μW when subjected with an acceleration of 10 m/s has been presented in [23]. In [24], an electrostatic KEH powered by a heartbeat-like signal is able to supply up to 57 μW with a variable capacitor in the range of 32 to 110 nF.

Nevertheless, in low amplitude vibration environments, where accelerations are well under 0.2 g, implementing this kind of energy harvesters becomes a very difficult endeavor.

1.1.3.3 Piezoelectric

In 1880, The Brothers Pierre and Jacques Curie are credited discovery of the piezoelectric effect in quartz crystals. The direct piezoelectric effect states that an electrical charge is generated when the material is subjected to a mechanical energy, whether delivered from compression, traction of vibration. In essence, piezoelectric KEHs use the capability of the piezoelectric materials to generate an electric field under mechanical deformation. Contrary to the electrostatic KEHs, no precharging is required. Piezoelectric harvesters based on aluminum nitride (AlN) have generated up to 60 μW, with less than 1 cm footprint [25]. Piezoelectric harvesters based on lead zirconate titanate (PZT) have obtained up to 40 μW [26]. These amounts of generated power, however, have been reported when the devices are unpacked. It is known that packaging affects the total output power of these devices drastically, making them less attractive from a real application perspective.

1.1.4 Fuel cells

Fuel cells (FCs) are devices that utilize an electrochemical process involving oxygen or another oxidizing agent to convert chemical energy of a fuel into electrical energy. Unlike a battery that stores energy, a fuel cell transforms chemical energy of its input fuel into electrical energy without the use of stored materials within its structure; thus, as long as reactants continue to flow, a fuel cell can theoretically produce continuous electrical power. Fuel cells are also different from typical heat engines because in the former, chemical energy is directly converted into electricity whereas in heat engines, an intermediate mechanical process must be performed. Fig. 1.4 shows the structure of a standard fuel cell.

Fuel cells are generally classified by the type of electrolyte they use, and its choice determines their operating temperature and the degree of fuel processing required. They exist in many different types and sizes, being able to generate up to hundreds of kW of power [27]. Some of the most popular technologies for fuel cells used nowadays are alkaline, phosphoric acid, molten carbonate and solid oxide. Their operating temperatures vary in between 200°C to 1000°C, limiting their applicability to large, external applications with

elaborated cooling and exhaust systems. Conventional fuel cells are regarded as low temperature if they operate in the region of 80°C and typically require expensive p-group catalysts [28]. However, biofuel cells are able to operate under mild conditions (20-40°C, near neutral pH), making them an attractive prospect for *in-vivo* applications [29].

The use of fuel cells exploiting species present into the human body to harvest energy for implantable biosensors offers considerable advantages. The constant presence and availability of the reactants directly into the body makes unnecessary external recharging mechanisms or replacement [13]. Among them, biofuel cells that use glucose as a reactant are perhaps the most studied, due to the abundance and availability of glucose in body fluids.

Glucose fuel cells can be divided into two groups depending on the catalyst used in the chemical reaction. The abiotically catalyzed group uses catalysts such as activated carbon or noble metals and have reached an output power of 50 μW/cm^2 during *in-vitro* experiments [31]. Experiments *in-vivo* realized on a dog generated 2.2 μW/cm^2 over a period of 30 days [32]. The enzymatically catalyzed group uses enzymes such as glucose oxidase or laccase in order

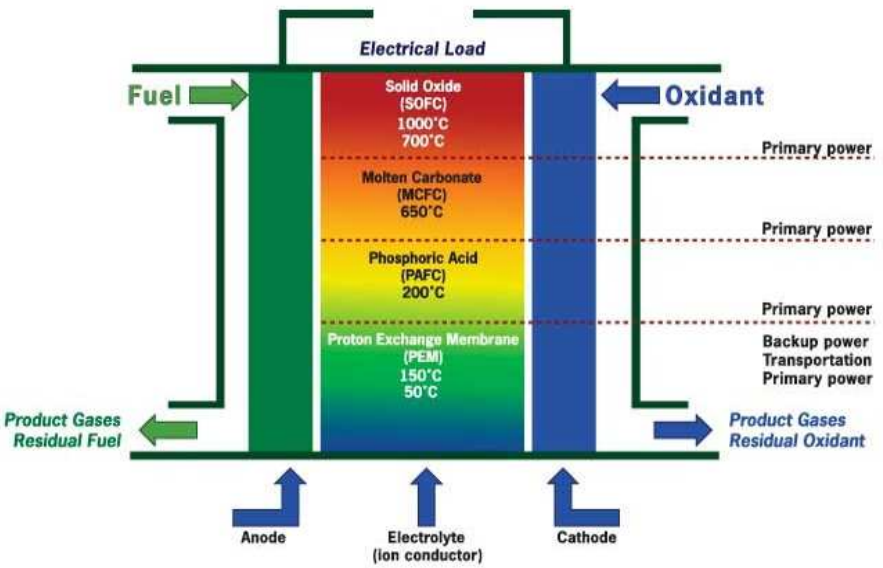

Figure 1.4: Typical fuel cell structure. Courtesy of [30].

to enable the electrode reactions. These devices are able to provide power densities as high as 430 $\mu W/cm^2$ [33], but the catalyst hast not lasted longer than a month [29].

The common denominator here is the short lifetime of the harvesters as a system, which is an undesirable characteristic if one is to consider fuel cells as a power source for implantable biosensors/stimulators with intented lifespans of years or decades. Additionally, the power density obtained in in-vivo tests is at least an order of magnitude less than that of *in-vitro*, reaching only units of microwatt.

1.1.5 RF harvesting

With the massification of mobile electronics and telecommunications, electromagnetic fields became ubiquitous. Radio frequency energy is emitted by sources that generate high electromagnetic fields such as TV stations, wireless radio networks and cell phone towers. With the aid of a receiving antenna and power management circuitry, RF harvesters are able to capture some of this "flying energy" to power electronic circuitry and/or recharge batteries. Nevertheless, ambient RF harvesting may not be a realistic approach in most situations since the available power density is typically too low [34].

Data presented in [35] show that the expected power densities from GSM base stations at a distance of 25-100 m range from 0.1 mW/m^2 to 1 mW/m2 whilst WLAN basestations provide at least one order of magnitude less. According to [36], the average RF power density is in the order of -12 dBm/m^2 ($\approx$ 63 $\mu W/m^2$). Thus, energy must be extracted at very low power densities, posing a very tight constraint in the power sensitivity of the receiver and the efficiency of the RF to DC converter. Moreover, RF ambient sources are very unreliable and should be used as a backup energy source only. Dedicated RF sources are another possibility and can help to tackle some of the previous problems. This approach is most commonly used as an application for RFID tags in which the sensing device wirelessly sends RF signals to a harvesting device which supplies just enough power to send back identification information specific to the item of interest.

Due to the omnidirectional nature of radiation, this technique is particularly well suited for batch tagging, where hundreds or thousand of tags are confined in a certain volume (e.g. a container or a storage facility). From the biomedical perspective, one certainly does not expect such a high density of elements and a lot of the transmitted power will be lost in tissue reflection and absorption. Therefore, bionic implants operate within close proximity of the base station

(typically 1–50 cm) and must be carefully designed to stay within the limits of the Specific Absorption Rate regulation.

In [37], an EH circuit using a 20 dBm, 4 GHz dedicated RF source transmitting to an on-chip loop antenna 7 cm away in free space is able harvest 0.5 μW. A device for deep brain stimulation presented in [38] claims to harvest 12-15 Joules per day using a undisclosed, dedicated RF source. The power consumption of this device is said to be 51 μW, corresponding to an energy consumption of 4.4 Joules per day. Assuming typical parameters of stimulation signals provided for Parkinson's disease (pulses of 2.5 V, 120 μs duration with a repetition rate of 185 pulses per second), the required amount of energy equals 0.2302 Joules per day, much less than the expected harvested energy per day. However, important data such as transmission power, distance and implant depth are not provided.

1.1.6 Biomimetic techniques

Most novel energy harvesting techniques base their principle of operation in natural processes in which energy storage and usage take place. In many of these works it is evident the strong analogies between complex electronic systems and biological energy management [39–41]. Natural photosynthesis allows plants to harvest and store energy by exploiting solar light as a source and CO_2 and water as reactants. Many attemps have been done to artificially reproduce the critical steps of this process. For example, a photosynthetic light conversion unit that mimics the light-harvesting process of phototropic bacteria is presented in [42]. Here, a self-assembled antenna aggregate mimics the supramolecular light-harvesting structures of phototropic bacteria while an embedded reaction center serves as an energy acceptor and charge transfer dyad. According to the authors, the unit can be seen as a conceptual approach to self-assembled (supra)molecular solar cells. It is claimed that the exciton transfer to the energy traps occurs in less than 40 ps and the emissions from the energy traps can reach efficiencies up to 90 % with an average lifetime of 14 ps. When compared with existing photovoltaic technologies, this short lifetime makes the process of collecting this emissions at the electrode side hard to accomplish.

Dye-sensitized solar cells are another type of energy harvester based on natural processes [43]. Its principle of operation also resembles photosyntesis by using a molecular dye that converts the incoming light in electrons that reach the cathode electrode via a liquid electrolyte. At the interface, the pair is splitted and electrons are collected at the anode by using a stratum of titanium oxide (TiO_2). The molecular dye plays the role of chlorophyll by converting light into

electrons while the electrolyte replaces the generated electrons (same role as water) and the TiO_2 mimics CO_2 working as the electron acceptor.

Both of the approaches presented above are very interesting and show promising results. However, from the point of view of implantable devices, they would suffer of the same drawbacks as any of the optical harvesting techniques presented in 1.1.1. Furthermore, they require more maturity to reach a marketable stage.

1.1.7 Electromagnetic coupling

Electromagnetic coupling can be made by means of inductive coupling or capacitive coupling. Each of these have certain characteristics that must be addressed independently. The main features of both techniques are explained below:

1.1.7.1 Capacitive coupling

Capacitive links benefit from the simplicity and low cost of capacitive interfaces, making them attractive for wireless charging stations. In [44], a capacitive link is able to transfer up to 3.7 W with more than 80% efficiency, using a series resonant converter constructed around the coupling capacitors. The system provides a peak efficiency of 84% at 3.2 W and 70% at 0.3 W load power. In addition the capacitive interface allows to confine the electromagnetic fields between the conductive plates, alleviating the need for magnetic flux guiding and shielding components that add bulk and cost to inductive solutions [45]. The major drawback of this approach is the required capacitance, which in turn limits the transfer range. In order to obtain the 156 pF of capacitance required, the parallel plates area must be approximately 45 cm^2 at distance of 250μm in free space. If the circuit was to operate at a distance of 1 cm, it would required around 0.17 m^2 (!) of parallel plates area.

1.1.7.2 Inductive coupling

The use of inductive links to power implanted sensors has been deeply investigated in the last decade. An inductive link consists of two coils. The primary coil is placed outside the body, generating a variable magnetic field by means of an alternate current flowing in it. The change of the magnetic flux through

the secondary coil generates an electromotive force across it, according to the Faraday-Neumann-Lenz law.

$$\epsilon = -\frac{d\phi B}{dt} \tag{1.2}$$

Where ϵ is the electromotive force generated by the change of the magnetic flux ϕB through the secondary coil. Using this method, power is transferred wirelessly through the body tissues, inducing an electromagnetic force in the implanted coil by means of an alternate current flowing on the external coil.

Inductive coupling present additional features, when compared with other kinds of power transmission. Exploiting this technique, data can be transmitted from outside to inside the body (downlink) and vice-versa (uplink) without using a radio-frequency transmitter or receiver.

Downlink transmission to the receiver side can be achieved by modulating the power signal. Amplitude-shift keying (ASK) is one of the most preferred modulation techniques due to its simplicity, allowing area and power reduction. A major drawback is that the transmission efficiency becomes suboptimal. Another solution for the downlink communication is frequency-shift keying (FSK). This technique allows a higher transmission rate when compared to ASK, but results in a more complex demodulator and increased difficulty of synchronization [46]. Uplink transmission is commonly achieved by means of the load-shift keying (LSK). By changing the impedance of the secondary circuit, the load seen by the primary circuit varies, provoking a change in the current flowing in the transmitter side. This change can be detected by an external demodulator, enabling uplink transmission without any internal RF transmitter [13].

Although most attention in literature is paid to power efficiency, there are two other very important metrics to consider when studying wireless power transfer. The first metric is the open circuit voltage at the receiver side and the second is how much power can be delivered to a miniature implant while still complying with the Specific Absorption Rate (SAR) regulations [47].

1.2 Specific Absorption Rate

Specific Absorption Rate (SAR) is a measure of the rate at which energy is absorbed by the body when exposed to a RF electromagnetic field; although,

it can also refer to absorption of other forms of energy by tissue, including ultrasound [48]. The IEEE Standard for safety levels with respect to human exposure to radio frequency EM fields defines the SAR as "the time derivative of the incremental energy (dW) absorbed by (dissipated in) an incremental mass (dm) contained in a volume element (dV) of given density (ρ)".

$$SAR = \frac{d}{dt}\left(\frac{dW}{dm}\right) = \frac{d}{dt}\left(\frac{dW}{\rho dV}\right) \tag{1.3}$$

The S.I. unit of SAR is watt per kilogram (W/kg). SAR can also be related to the temperature increase at a point by:

$$SAR = \left(\frac{c\Delta T}{\Delta t}\right)_{t=0} \tag{1.4}$$

Where ΔT is the change in temperature (°C), Δt is the duration of exposure (s) and c is the specific heat capacity of the tissue (J/kg°C). SAR is usually averaged either over the whole body, or over a small sample volume (typically 1 g or 10 g of tissue). The value cited is then the maximum level measured in the body part studied over the stated volume or mass. It is commonly used to measure power absorbed from mobile phones and during MRI scans. The value will depend heavily on the geometry of the part of the body that is exposed to the RF energy, and on the exact location and geometry of the RF source. Thus tests must be made with each specific source, such as a mobile phone model, and at the intended position of use. For example, when measuring the SAR due to a mobile phone; the phone is placed at the head in a talk position. The SAR value is then measured at the location that has the highest absorption rate in the entire head, which in the case of a mobile phone is often as close to the phone's antenna as possible.

1.3 Wireless Power Consortium

In consumer electronics, the power cord has been regarded as "the final cord" that needs to be eliminated in order to get a true wireless user experience [49]. Founded in December 2008, the Wireless Power Consortium targets to establish a global standard for wireless charging that finally enables to reach this goal. The "Qi" standard interface has been designed to deliver inductive electrical power for distances up to 4 cm.

Currently, the low power standard (5 W) has been fully developed and the consortium is aiming to standardize fast charging ports for mobile devices (10-15 W) and the "the cordless kitchen", a concept which requires power up to 2 kW.

Its principle of operation is based on inductive coupling as shown in 1.5. It consists of a transmitter coil L1 and a receiver coil L2, which are magnetically coupled. An alternating current in the transmitter side generates a magnetic field which induces a voltage in the receiver coil. This voltage can then be used to power a device or to recharge a battery.

Roughly speaking, the efficiency of such a system depends on the coupling factor k between the inductors and their quaility factor Q. The coupling is determined by the distance between the coils, their aspect ratio, the shape and the misalignment.

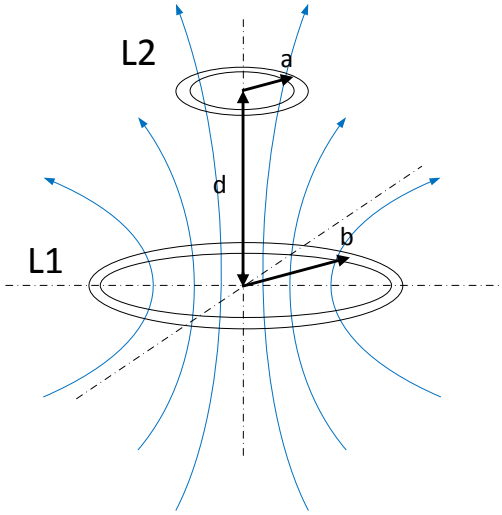

Figure 1.5: Simple representation of an inductively coupled power transfer system.

1.4 Current Scenario

Currently, neurostimulators are about the size of a stopwatch and are implanted in the chest or abdominal area, from where leads are sent to the area to be stimulated (spine or brain). Fig. 1.6 illustrates one of these devices as presented in [50]. The bulky components located in the chest correspond to the battery

and the power management system required to provide the required energy for stimulation.

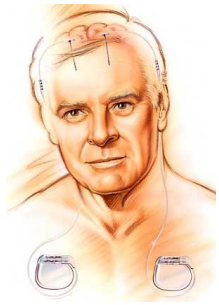

Figure 1.6: Deep brain stimulator for Parkinson's relief. Courtesy of [50].

Neurostimulators must be replaced periodically upon battery failure, (usually within three to five years) though battery life is dependent on individual usage. Battery life can be reasonably predicted by the use of a telemetry programming device so that the unit can be replaced prior to battery failure. Rechargeable devices are now commonly implanted with a battery life in the range of 10 to 15 years dependent on use.

In the future, it is expected that these devices would further reduce power consumption and volume. Some neuroscientists say that they could implant a fully operative neurostimulator (this is, including all power management and storage) as big as a 2 euro coins inside the skull (see Fig. 1.7). Having this possibility would significantly improve patient's comfort by allowing more freedom of movement. We foresee a scenario in which energy can be transmitted to the patient's implant during the time the person is likely to maintain a fixed position (e.g. while sleeping or in his/her chair at work), so that the battery or storage element used is continuously recharged, extending the device's lifetime.

Figure 1.7: A two euro coin.

1.5 Research Objectives

This thesis focuses on energy harvesting using magnetic coupling (inductive links). The main goal is to establish the feasibility of larger distance ($\approx$ 10 cm range) wireless power transfer to biomedical implants under non-ideal spatial conditions (i.e. misaligned coils), while complying with SAR regulations. The following research tasks must be completed in order to answer the research question:

- Model the inductive link in free space under misaligned conditions.
- Study biological tissue and determine its influence on power transfer.
- Analyze safety conditions under current EMF regulations.
- Realize a circuit level design of the near-field inductive link.
- Realize a circuit level design of the rectifier and the power management unit.

1.6 Thesis Outline

The thesis is organized as follows. An in-depth study of near-field wireless power transfer using inductive links is presented in Chapter Two. Here, a definition of the near-field region and its characteristics is introduced. With this background, a generalized model of an inductive link is developed, which allows us to study how distance and size ratio affect system's performance. Furthermore, the effect of coils misalignment is analyzed, as well as the consequences of resonant and non-resonant operation. Chapter Three introduces the electrical properties of human tissue, and the results of Chapter Two are tested within this new environment in order to determine how the power transmission is affected by different channel compositions and determine the specifications; i.e. maximum available power, EMF regulation compliance and operating frequency range. Chapter Four deals with the link design and power receiver design, which includes the transmitter, the inductive link, the rectifier and the power management unit. The objective is to obtain a system with good power sensitivity and efficiency. Simulations results of the aforementioned circuitry are shown in Chapter Five, including robustness via corners simulations. The thesis contribution, conclusions and recommendations are given in the last part of the book.

Chapter 2

Study of Inductively Coupled Interfaces

More often than not, when referring to wireless power transfer, different technologies are agglutinated, leading to errors studying their characteristics and impact. Understanding the differences between near and far field wireless power is of great importance when addressing this topic, not only at the engineering level but also for the general public.

In this chapter, a clear differentiation between near and far field is introduced, which paves the way for the description and analysis of inductively coupled interfaces for power transfer. The characterization and modeling of such systems will allow us to better understand the mechanisms involved in the transmission of energy and how this is affected by the geometry of the coils and the particular spatial conditions of the link such as distance and angle misalignment.

2.1 Near and Far Field Regions

The space surrounding an antenna is usually subdivided into three regions; the reactive near field region, the radiating near field (referred to as the Fresnel)

region and the far field or Fraunhofer region. These regions are designed to identify the change in the field structure as the observation point is crossing between boundaries. For an electrically small antenna[1] there are only two separate regions, the reactive near field and the radiating field [51]. Typically, the boundary between these two regions is assumed to be a distance r from the antenna, defined as:

$$r = \frac{\lambda}{2\pi} \tag{2.1}$$

In the case of an electrically large antenna a further distinction becomes significant where the radiating field is split into the radiating near field and the radiating far field. Figure 2.1 presents an illustration of the different regions as a function of the wavelength.

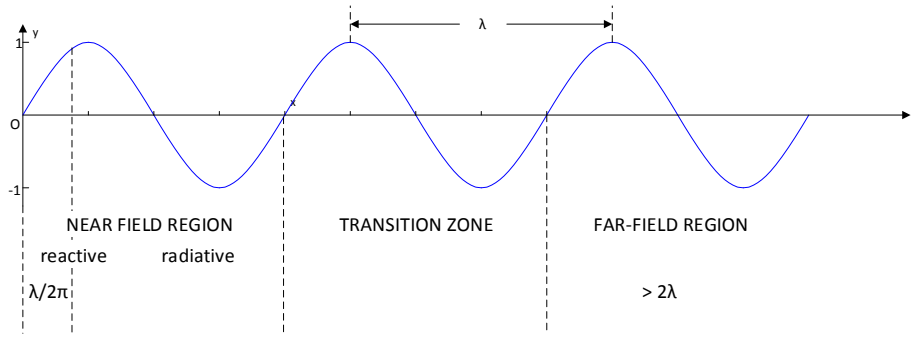

Figure 2.1: Typical EM region definition as a function of wavelength.

In order to illustrate the difference between the three field regions, we can consider the magnetic field of a small loop antenna. At a radial distance r from a circular loop carrying a sinusoidal uniform current $I = I_o e^{jwt}$, two components of magnetic field exist, being H_θ and H_r [51, 52], expressed as:

$$H_\theta = \frac{m_o sin(\theta) e^{j(wt-\beta r)}}{4\pi} \left(-\frac{\beta_o^2}{r} + j\frac{\beta_o}{r^2} + \frac{1}{r^3} \right) \tag{2.2}$$

$$H_r = \frac{m_o cos(\theta) e^{j(wt-\beta r)}}{4\pi} \left(j\frac{\beta_o}{r^2} + \frac{1}{r^3} \right) \tag{2.3}$$

[1] An antenna is considered electrically small if the total conductor length is less than a tenth of the wavelength.

where m_o is the magnetic moment, equal to $I_o \pi a^2$ and β_o is defined as the phase constant of free-space and is equal to $2\pi/\lambda_o$. The terms composing the magnetic field are typically referred to as follows [51]:

- $\frac{1}{r}$, radiation component in the far field.
- $\frac{1}{r^2}$, induction component in the radiating near field.
- $\frac{1}{r^3}$, magnetostatic component in the reactive near field.

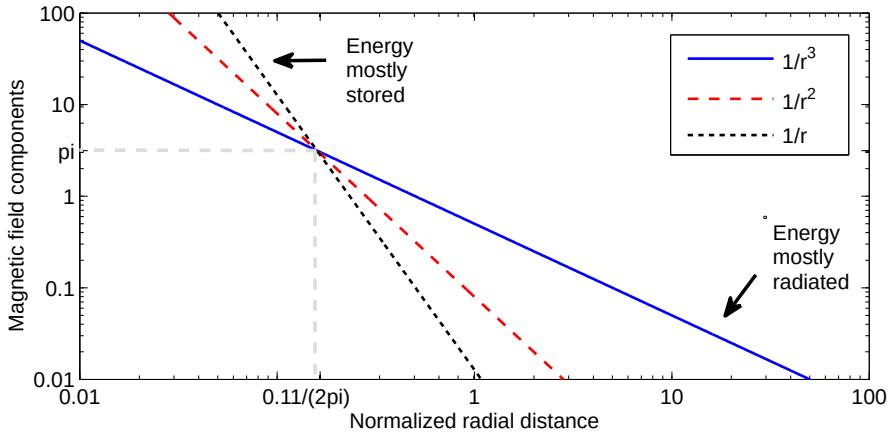

Figure 2.2: Variation in the H-field components vs. normalized radial distance.

Fig. 2.2 illustrates the variation of the components in the magnetic field as a function of the distance, normalized to the wavelength at the operating frequency. Solving Maxwell's equations for the fields of a localized oscillating source like an antenna, surrounded by a homogeneous and isotropic material, the field decays proportionally to the terms presented above [51]. In this conditions, the fields can be expressed as a multi-pole expansion. The terms in this expansion are spherical harmonics, providing the angular dependence, multiplied by spherical Bessel functions, supporting the radial dependence. For large r, the spherical Bessel functions decay as $1/r$ in the radiating far field. For a distance closer to the source, the reactive near field starts to take over and higher powers of r become relevant. Initially, the term dependent on $1/r^2$ kicks in, frequently referred as the induction term of the radiating near field. If r continues decreasing, the term $1/r^3$, referred as the magnetostatic field term dominates. At a distance shorter than $\lambda/2\pi$ the magnetic field dominates.

In the more realistic systems, the reactive near field is composed of inductive, electrostatic, electric and magnetic fields along with some intrinsic but limited radiated energy (due to accelerated charges in the inductor). These are all related in very complex relations, although the predominant fields are reactive. Because of this, studying their individual characteristics in this near field is extremely difficult and provides very little insight [53].

2.2 Loop antenna

The loop antenna is a fundamental and simple antenna and it has received tremendous attention for short-range wireless power transfer and communications. Due to their smaller size, loop antennas have been used continually since the early days of radio and they have become particularly widespread for applications in the HF band (3-30 MHz) [54].

The loop antenna has been identified as being particularly suited to applications where wireless power delivery is required such as the powering of biomedical implants and passive RFID tags [55–58]. The use of a loop antenna in near field systems yields several advantages, among these being [51, 54]:

- The relatively non-directional nature of loop antennas can impreve the operating range of the device in the near field.
- In the HF band the antenna may be reasonably described as electrically small allowing the assumption of uniform current distribution, which significantly simplifies the analysis.
- The effect of any conductive media, such as biological tissue, is decreased using an implantable loop antenna due to the fact that the dominant magnetic near field suffers less attenuation compared to an electric field. This particular feature will be discussed in more detail in Ch. 3.
- A small loop is primarily inductive. In most magnetically coupled systems, resonance is employed using the inductance of the loop antenna in a resonant tank. In this manner, the loop can operate as a transmitting and receiving antenna, at the specified resonant frequency. This is demonstrated in simple low power short range transmitters [51].

The loop antenna is a very versatile structure classified into two categories: (a) electrically small and (b) electrically large. A loop antenna is considered to

be electrically small if the radius is very small compared to the wavelength (a << λ) or the overall length l is less than one tenth of a wavelength (l <$\lambda/10$).

As demonstrated by [59], the radiation resistance of a loop antenna can be expressed as:

$$R_{RAD} = 20\pi^2 N^2 \left(\frac{l}{\lambda}\right)^4 \Omega \tag{2.4}$$

where N is the number of turns of the antenna, l is the circumference of the loop and λ is the wavelength. The radiation and ohmic losses are important parameters in the design of an antenna as they determine the radiation efficiency. In general, for electrically small loop antennas the loss resistance is generally much larger than the radiation resistance [51]. As a consequence, the corresponding radiation efficiency is very low and thus, they are rarely employed in conventional far field transmission. When employing loop antennas, magnetic coupling is a more efficient method to transfer energy in the near field [54].

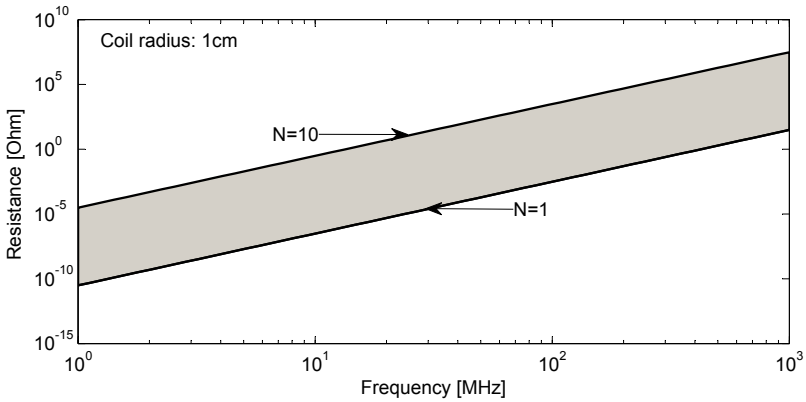

Figure 2.3: Radiation resistance for a loop antenna with respect to frequency.

2.3 Mutual Inductance of Loop Coils

The approach presented here is based on the studies and results of Soma *et.al.* [60], Fotopoulou and Flynn [61] and Dionigi *etal.* [62]. For a more extensive

mathematical treatment of self inductances and mutual inductances of different geometries, the reader can refer to the work of de Queiroz presented in [63].

The mutual inductance between two circular current filaments can be calculated by Neumann's formula:

$$M = \frac{\mu_0}{4\pi} \iint \left(\frac{\vec{ds} \,.\, \vec{ds'}}{r} \right) \tag{2.5}$$

where ds and ds' are incremental sections of the filaments and the dot means the scalar product between them. The exact integral is obtained from an adequate parametrization of the geometry of the filaments. As of the case of two coaxial circles with radius a and b, with a distance d between the centers, the mutual inductance can be calculated as:

$$M = \frac{\mu_0}{4\pi} \iint \frac{cos(\epsilon)}{r} ds ds' \tag{2.6}$$

where,

$$r = \sqrt{a^2 + b^2 + d^2 - 2ab\ cos(\varphi - \varphi')} \tag{2.7a}$$
$$\epsilon = \varphi - \varphi' \tag{2.7b}$$
$$ds = a\ d\varphi \tag{2.7c}$$
$$ds' = b\ d\varphi' \tag{2.7d}$$

From here, it is possible to express the mutual inductance as:

$$M = \frac{\mu_0}{4\pi} \int_0^{2\pi} \int_0^{2\pi} \frac{ab\ cos(\varphi - \varphi') d\varphi d\varphi'}{\sqrt{a^2 + b^2 + d^2 - 2ab\ cos(\varphi - \varphi')}} \tag{2.8}$$

This integral can be exactly solved in the form:

$$M = -\mu_0 \sqrt{ab} \left[\left(m - \frac{2}{m} \right) K + \frac{2}{m} E \right] \tag{2.9}$$

where K and E are the complete elliptic integrals of the first and second kind, defined as:

$$K = F(m, \pi/2) = F(m) = \int_0^{\frac{\pi}{2}} \frac{d\varphi}{\sqrt{1 - m^2 sin^2(\varphi)}} \tag{2.10}$$

$$E = F(m, \pi/2) = E(m) = \int_0^{\frac{\pi}{2}} \sqrt{1 - m^2 sin^2(\varphi)}\ d\varphi \tag{2.11}$$

and m is the modulus of the elliptic integrals given by:

$$m = \frac{2\sqrt{ab}}{\sqrt{(a+b)^2 + d^2}} \tag{2.12}$$

When the coils are considered as current sheets, the coupling coefficient can be effectively expressed as:

$$k = \frac{M}{\sqrt{L_1 L_2}} \tag{2.13}$$

Using the aforementioned, a MATLAB script to visualize the coupling factor as function of coil distance and size ratios[2] is made (see appendix A) and the results are shown in Fig. 2.4. Note that the x and y-axis are given in units relative to the receiver coil radius, which in this case is set to 1.2 cm (2 euro coin).

The contour plot of Fig. 2.4(b) allows to visualize the patterns in which the coupling factor changes as function of transmiter size and distance. The figure suggests that for a given distance between the coils, there is an optimal size ratio that induces the highest coupling factor. This can be observed more clearly in Fig. 2.5. Here, the coupling factor is plotted against the mutual

[2]The distance and size ratios are defined as d/b and a/b, where b corresponds to the receiver radius.

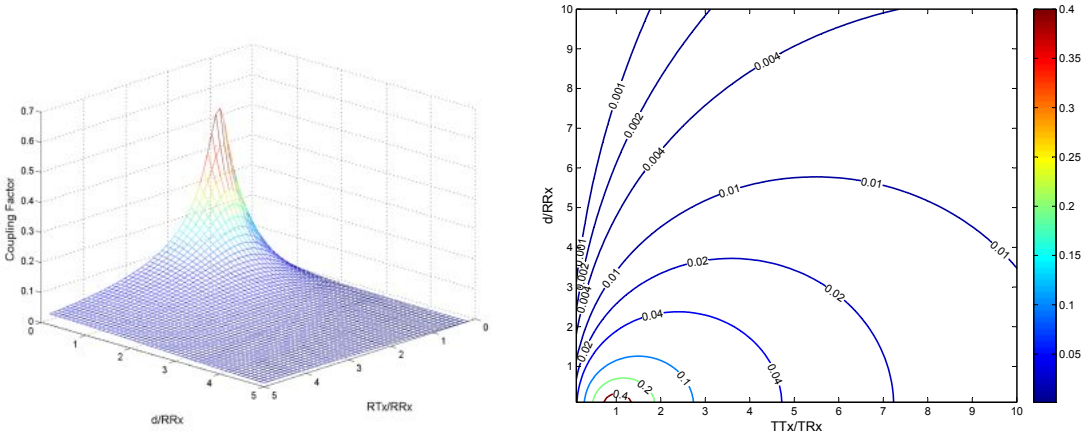

(a) Surface plot.

(b) Contour plot.

Figure 2.4: Coupling factor as a function of distance and coils ratio.

inductance for several d/b values. The size ratio increases in the direction of the arrow in the graph. For shorter distances (e.g. red solid line) we can see that the coupling factor increases as the size ratio increases but eventually reaches a maximum. Further increasing the size ratio no longer provides a beneficial effect. At longer distances, the impact of this effect is still present but is much less pronounced (e.g. black dash-dotted line) as the separation of the coils becomes the dominant factor in the link.

2.4 Resonant operation

In this section, the difference between resonant and non-resonant operation of the receiver is studied. To generalize the results, the parameter definitions of [64] are used. Table 2.1 summarizes the required terms.

To investigate the performance of the system under resonant and non-resonant operation, the losses in the coils are determined and related to the output power as loss factors. The system quality factor Q is the geometric average of the transmitter and receiver quality factors. The factor q defines their ratio (see Table 2.1).

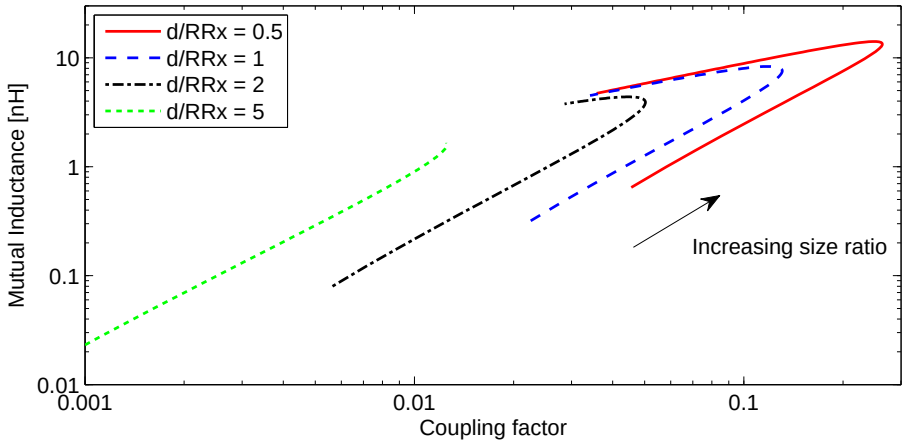

Figure 2.5: Coupling factor vs. mutual inductance.

Table 2.1: near field inductive link parameter definition.

Definition	Symbol	Equation
Receiver loss factor	λ_{Rx}	$\frac{P_{Loss_{Rx}}}{P_{OUT}}$
Transmitter loss factor	λ_{Tx}	$\frac{P_{Loss_{Tx}}}{P_{OUT}}$
Matching factor	γ	$\frac{R_L}{Z_C}$
Receiver quality factor	Q_{Rx}	$\frac{wL_{Rx}}{R_{Rx}}$
Transmitter quality factor	Q_{Tx}	$\frac{wL_{Tx}}{R_{Tx}}$
System quality factor	Q	$\sqrt{Q_{Rx}Q_{Tx}}$
Quality factor ratio	q	$\sqrt{\frac{Q_{Rx}}{Q_{Tx}}}$
Capacitance factor	χ	$\frac{Z_C}{wC_{Rx}}$
Characteristic impedance	Z_C	wL_{Rx}

Considering this, the receiver loss factor can be expressed as:

$$\lambda_{Rx} = \frac{1}{qQ\gamma} \tag{2.14}$$

In a similar way, the transmitter loss factor is given by:

$$\lambda_{Tx} = \frac{q}{k^2 Q\gamma}\left[\left(\gamma + \frac{1}{qQ}\right)^2 + (1-\chi)^2\right] \tag{2.15}$$

The optimal operating condition for a given load is determined by setting $\mathrm{d}\lambda_{Tx}/\mathrm{d}\chi$ to zero and solving for χ, which leads to a value of $\chi = 1$. This result corresponds to the condition in which inductive reactance is effectively compensated by a capacitive reactance (i.e. resonant condition). It is independent of the coupling factor and the load impedance, thus a fixed capacitor is optimal for all operation cases [64].

If the optimal resonant matching is used, the expression of the transmitter loss factor reduces to:

$$\lambda_{Tx} = \frac{1}{(Qk)^2}\left(\sqrt{\gamma qQ} + \frac{1}{\sqrt{\gamma qQ}}\right)^2 \tag{2.16}$$

The total loss factor then becomes:

$$\lambda = \frac{1}{\gamma qQ} + \frac{1}{(Qk)^2}\left(\gamma qQ + \frac{1}{\gamma qQ} + 2\right) \tag{2.17}$$

Fig. 2.6 presents the variation of λ as a function of γ for two links. The red solid lines correspond to resonance ($\chi = 1$) while the blue dashed lines represent the systems not at resonance ($\chi = 0$). Both in Fig. 2.6(a) and Fig. 2.6(b) the product Qk (which can serve as the FoM of the link) is maintained equal.

Fig. 2.6(a) shows that by operating at resonance, the link has a better performance (*i.e.* lower λ). This improvement is even more pronounced for the low coupling condition, such as in Fig. 2.6(b). Here, resonant operation provides a loss factor about 10x smaller than in the non-resonant case.

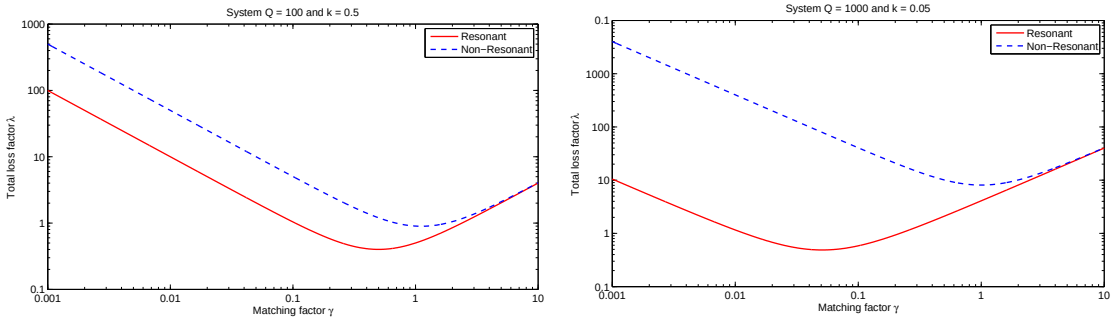

(a) Low Q, high k. $Qk = 50$

(b) High Q, low k. $Qk = 50$.

Figure 2.6: Link operation for different combinations of Q and k.

Fig. 2.7 studies the effect of different quality factors in the transmitter and receiver, while maintaining the same coupling (0.1). In Fig. 2.7(a) we analyze a system in which the transmitter has a higher quality factor (300) compared to the receiver (40). In terms of loss factor, resonant operation presents a performance slightly less than a decade better than the non-resonant case.

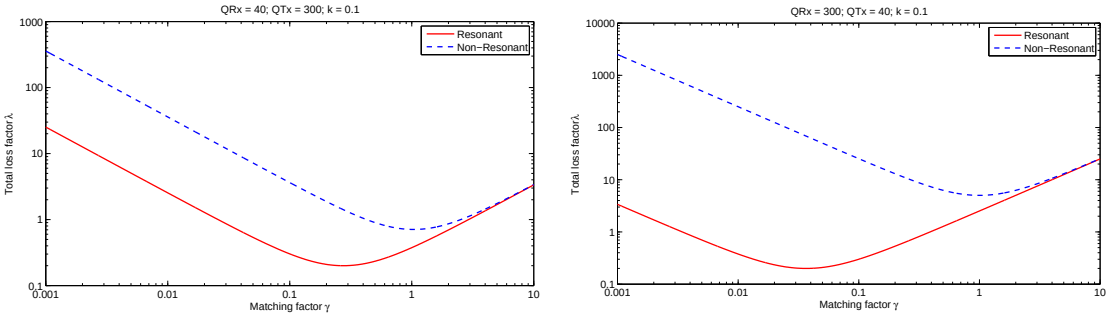

(a) High Q_{Tx}, low Q_{Rx}

(b) Low Q_{Tx}, high Q_{Rx}

Figure 2.7: Link operation for high and low Q in the transmitter and receiver.

If however, the coils could be interchanged, placing the better at the receiver side, as shown in Fig. 2.7(b), we could observe a larger difference in performance between resonant and non-resonant operation. While the resonant case kept its optimal loss factor the same, the non-resonant operation degraded its own significantly. These results can prove themselves important in the system design from an economic perspective.

In biomedical applications, typically the receiver side is tightly constrained in terms of area and volume. If one is to design a link using a coil array at the transmitter side, using low(er) quality factors can help to reduce costs. The receiver can be implemented with a single, high quality factor coil.

For optimal resonant matching Fig. 2.8 depicts the variation of λ with respect to γ for a set of different coupling factors ranging from 0.01 to 0.2. It is seen that the optimal matching factor shifts downwards as the coupling coefficient lowers. Indeed, for any given k, the optimal γ can extracted from Eq. 2.17 by setting its derivative to zero. Solving it yields:

$$\gamma_{opt} = \frac{1}{qQ}\sqrt{(kQ)^2+1} \tag{2.18}$$

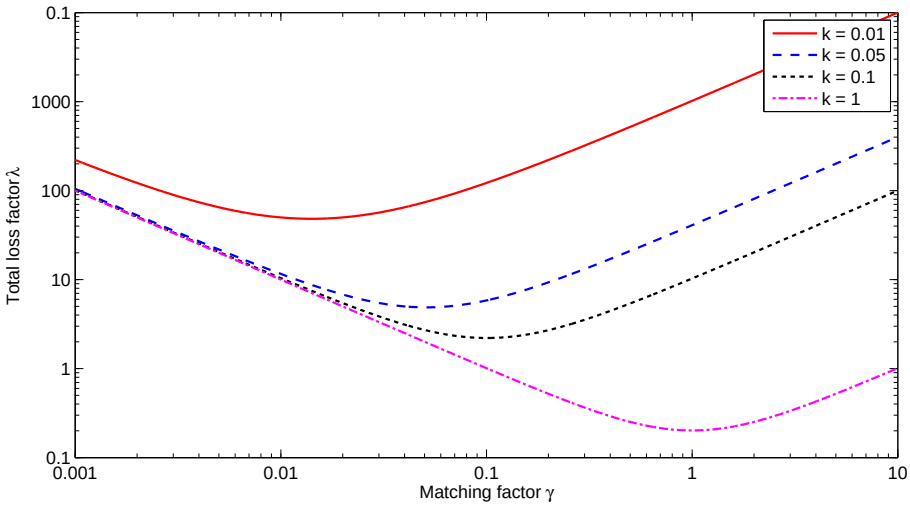

Figure 2.8: Matching factor vs. Loss factor for different k.

Replacing γ_{opt} in Eq. 2.17 gives the minimum achievable loss factor:

$$\lambda_{min} = \frac{1}{(kQ)^2}\left[2+\sqrt{(kQ)^2+1}+\frac{1}{\sqrt{(kQ)^2+1}}\right]+\frac{1}{\sqrt{(kQ)^2+1}} \tag{2.19}$$

which can be simplified to:

$$\lambda_{min} = \frac{2}{(Qk)^2}\left(1 + \sqrt{1 + (Qk)^2}\right) \tag{2.20}$$

A curve that illustrates the loss factor with respect to the figure of merit kQ is shown in Fig. 2.9. Using this graph one can quickly estimate the trade-off between device quality and performance at a given coupling (related to distance). The feasibility region is defined above the line. Depending on the application, physical limitations and budget, certain maximal performance can be obtained. Beyond this limit the near field inductive link technology does not provide a feasible solution with the current state of developments.

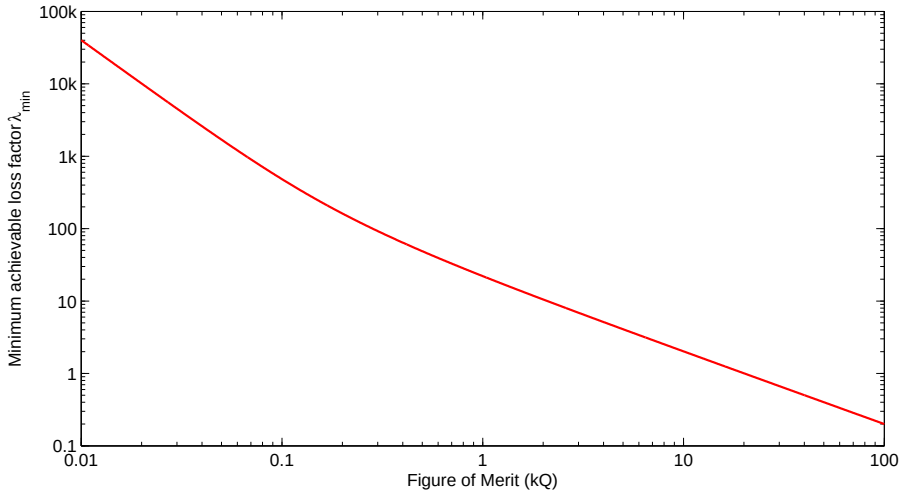

Figure 2.9: Loss factor with respect to the kQ product.

2.5 Efficiency

Using the results from Secs. 2.3 and 2.4, it is possible to estimate the efficiency of a near field inductive wireless power transfer system. Let us define the efficiency of the system as:

$$\eta = \frac{1}{1 + \lambda} \tag{2.21}$$

Here, only the losses in the magnetic system are considered. Losses in the generator and rectifier are comparable to any other power converter and will be addressed in detail in Ch. 4. Depending on the distance and the size ratio, one can obtain a certain value of coupling factor. With this coupling and assuming reasonable quality factors, the efficiency of the link can be determined by using Eq. 2.21. For consumer and biomedical applications, quality factors in the order of hundreds can be expected in the low MHz range [57, 60–65].

Fig. 2.10 illustrates the overall system efficiency estimation for different size ratios with respect to the coils distance. Qualitatively speaking, several conclusions can be drawn from here. Naturally, the shorter the distance between the coils, the higher the attainable efficiency. However, we can observe that for distances of one receiver radius or less, size ratios close to unity predict higher efficiencies (dash dotted red and dotted magenta lines). As the distance becomes larger, bigger size ratios outperform the others. For instance, when the distance is greater than 4X the receiver radius, a transmitter with 5X size ratio (blue dashed line) would offer a better efficiency than any of the other ratios plotted.

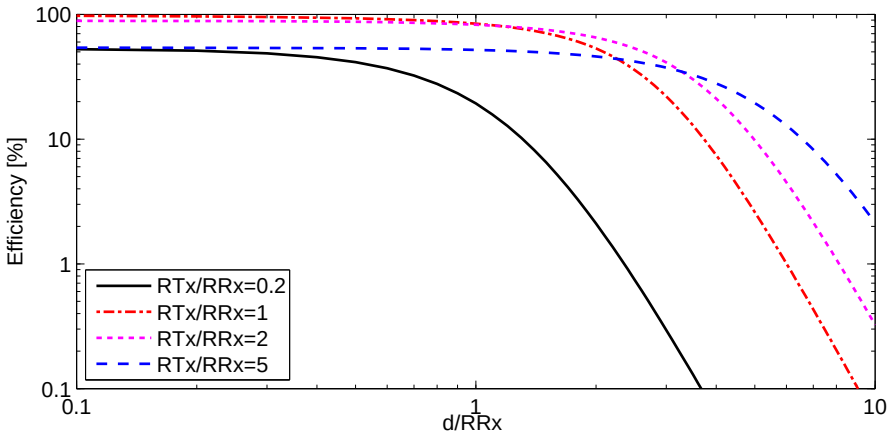

Figure 2.10: Maximum achievable efficiency vs. coil separation.

Considering that in our application there is not a fixed distance, a decision must be made regarding the size ratio based on the expected average operating condition. Moreover, one can already have an idea of the achievable efficiencies before diving into complex circuit design. As mentioned by Waffenschmidt in [65], near field inductive power transmission for very short distances can compete with conventional power supplies technologies at any power level. However, due to fundamental limitations, it is very unlikely to extend this

technology to high power, long distance applications. On the other hand, biomedical devices fall in the low power category and can still benefit from this technology at a range of several centimeters.

2.5.1 Power Limits due to EMF Regulations

Another constraint in the design of wireless power transfer interfaces is the one that has to do with the regulations limiting the levels of time-varying electric, magnetic and electromagnetic fields. Using the restrictions available in [66] and [67] for general public exposure one can estimate the maximum power output of the link.

Consider a circular loop inductor penetrated by a magnetic flux ϕ_{Tx}. If the magnetic flux density B_{Tx} is homogeneous over the area of the loop A, as is the case in poorly coupled systems [51], the output voltage V_{OUT} is equal to the induced voltage:

$$V_{ind} = NAjwB_{Tx} \tag{2.22}$$

where N is the number of loops of the coil. If properly matched, the maximum power that can be extracted is expressed as [65]:

$$P_{max} = Q\frac{(|V_{ind}|)^2}{4wL_{Rx}} \tag{2.23}$$

Defining AL as the inductance scaled to one turn with $L_{Rx} = N^2AL$, the maximum output power can be directly calculated from the magnetic flux density B_{Tx} as shown below:

$$P_{max} = Q\frac{w}{4}\frac{(A\,|B_{Tx}|^2)}{AL} \tag{2.24}$$

Fig. 2.11 presents the estimated maximum output power subject to the EMF regulations for a single turn receiver coil of 1.2 cm radius. The quality factor of the coil is recalculated for every frequency and the influence of radiation resistance is also considered. Although the calculated values shall not be regarded as exact, they still give a good estimation of the order of magnitude of

the power level. The red dashed line in the curve corresponds to frequencies in which the system cannot longer be considered exclusively magnetic. The drop that occurs around 300 MHz is due to the impact of the radiation resistance at these frequencies. Between 100 kHz and 30 MHz the estimated maximum power is close to 50 mW.

When considering an implantable device, safety becomes of utmost importance. Since the distance between coils could change, the power levels have to be adapted accordingly to stay below the safety limits.

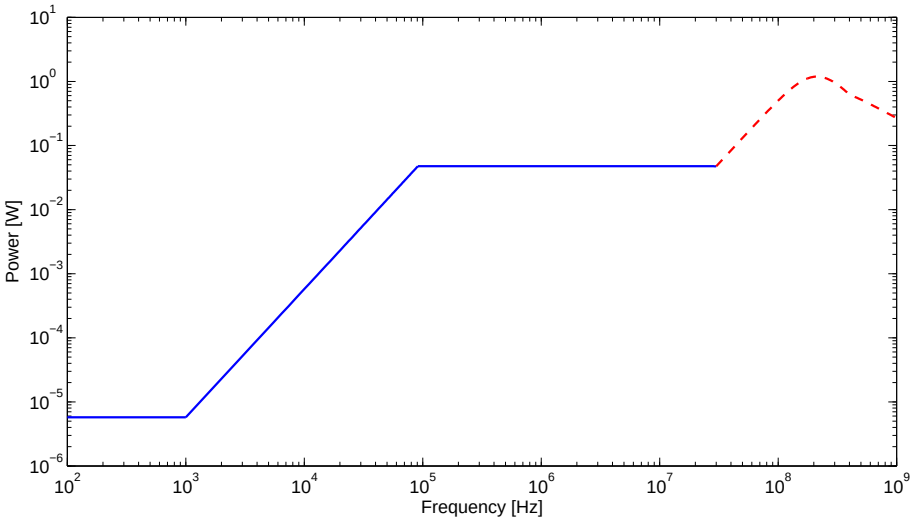

Figure 2.11: Estimated Maximum Output with EMF limits

2.6 Misalignment

In the previous sections there has been much talk about distance variation and uncertainty in the position between the transmitter and receiver. Nevertheless, so far only coaxial variations have been taken into account. In this section the lateral and angular misalignment are introduced to see how they affect the performance of the link. For simplicity, the lateral misalignment is constrained to 1 receiver radius.

Fig. 2.12 shows the two scenarios studied for the misalignment case. Of course it is possible to have an operating condition in which both lateral and angular

misalignment happen, but implementing a mathematical model including both effects simultaneously would be cumbersome and bring little benefit.

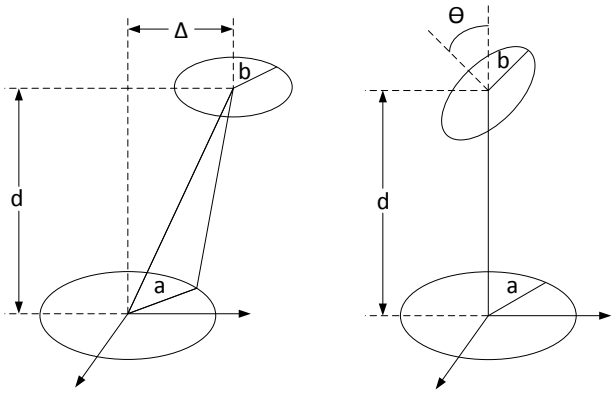

(a) Lateral. (b) Angular.

Figure 2.12: Coil misalignment cases studied.

Based on the results for the coaxial scenario, Soma *etal*. derived expressions for the case of lateral and angular misalignment. Let us define $G(m)$ as:

$$G(m) = m - \left(\frac{2}{m}\right) K + \frac{2}{m} E \tag{2.25}$$

It is possible to determine upper and lower boundaries for the mutual inductance. For the lateral case these are given as:

$$M_{min} = \frac{\mu_0 ab}{\sqrt{a(b+\Delta)}} G(m_{min}) \tag{2.26}$$

$$M_{max} = \frac{\mu_0 ab}{\sqrt{a(b-\Delta)}} G(m_{max}) \tag{2.27}$$

$$m_{min} = \sqrt{\left(\frac{4a(b-\Delta)}{(a+b-\Delta)^2 + d^2}\right)} \tag{2.28}$$

$$m_{max} = \sqrt{\left(\frac{4a(b+\Delta)}{(a+b+\Delta)^2+d^2}\right)} \tag{2.29}$$

Similarly, for the angular case:

$$M_{min} = \frac{\mu_0\sqrt{ab}}{\sqrt{cos(\alpha)}} G(m_{min/max}) \tag{2.30}$$

$$m_{min} = \left(\frac{4ab\,cos(\alpha)}{a^2+b^2+d^2-2bd\,sin(\alpha)+2ab\,cos(\alpha)}\right) \tag{2.31}$$

$$m_{max} = \left(\frac{4ab\,cos(\alpha)}{a^2+b^2+d^2+2bd\,sin(\alpha)+2ab\,cos(\alpha)}\right) \tag{2.32}$$

Fig. 2.13 presents the results of implementing the effects of lateral and angular variations in the performance of the link. There exist certain similarities between them that are worth stressing. In both cases, the influence of the misalignment loses importance as the distance increases. Only for really short distances (less than 1 receiver radius) the impact on the coupling factor is significant. For the system envisioned, this is a very rare operating condition. Still, if it were to occur, the coupling factors at this very short distances are higher than the average operating distance and the system would be able to still operate properly.

2.7 Summary

In this chapter, we have described in detail the near field inductive interfaces and analyzed their performance limitations. A clear line is drawn separating near and far field, avoiding any misconceptions that may arise when referring to the broader wireless power field. From here, we analyzed inductive link interfaces via the modeling of self and mutual inductors and the coupling factor with respect to the spatial conditions. This allows us to predict to a certain extent the performance of the system and find its fundamental limits, which in turn enhances the understanding of the technology. By parameterizing the link and the models with respect to a reference dimension, the results obtained here are applicable to any size geometry without loss of generality.

In particular, the receiver radius has been fixed to 1.2 cm (a 2 euro coin) and from here, results can be extracted. For a coil-to-coil distance of 10 cm, coupling factors in the range of 0.01 to 0.001 can be expected. This inevitably harms the performance of the system as we have seen in the loss factor and ultimately in efficiency. Resonance becomes an important tool to overcome some of the limitations encountered and should be used, especially at very low coupling factor condition. The maximum feasible estimated output power of 50 mW makes possible the usage of this technique for low power applications such as biomedical devices. However, safety comes first and care must be taken not to surpass the regulations limiting the time-varying EM fields.

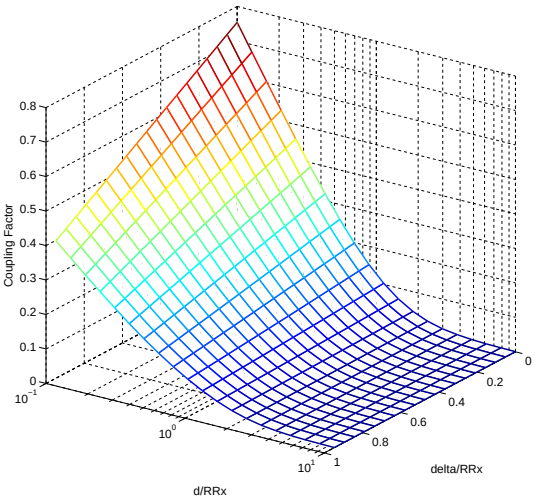

(a) Surface plot.

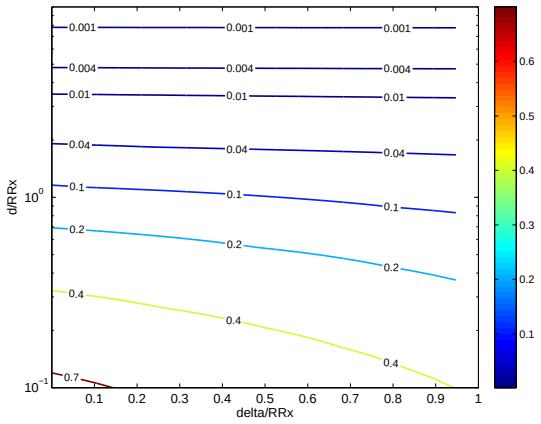

(b) Contour plot.

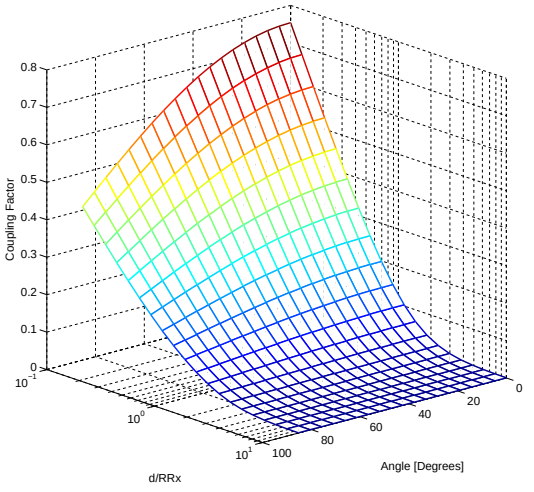

(c) Surface plot.

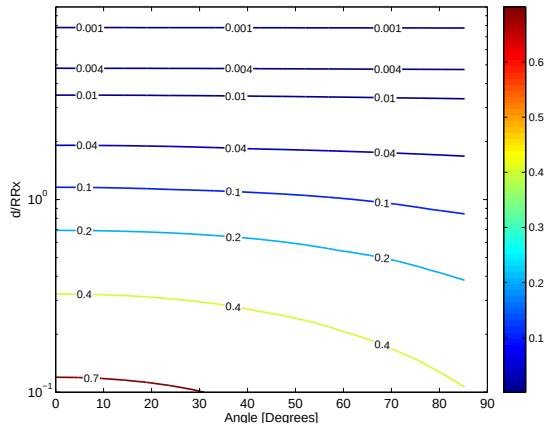

(d) Contour plot.

Figure 2.13: Effect of angular and lateral misalignment.

Chapter 3

Impact of Biological Tissue on Near-Field WPT

To date, attention has been mostly given to the characterization of the effects of electric fields on tissues; little to no attention has been paid to the effects of tissues on the performance of near-field inductive links [68]. Many publications have assumed far-field propagation while in fact the system they describe operates in the near field region. In this chapter, we focus in how magnetic field is coupled through biological media and analyze the specific absorption rate and tissue heating with respect to frequency.

3.1 Dispersive Materials

In many applications, one can obtain sufficiently accurate results by considering that material parameters are constants. However, constant material parameters are just an approximation. When the speed of light in a material is a function of frequency (i.e. variable permeability and/or permitivity), the material is said to be dispersive [69]. The body is composed of tissues which behave as a lossy dielectric material and in order to assess properly its impact on the link, we need to understand its nature. Among the models available for biological

tissue, Debye models are widely used for computational analysis and easily available for use.

3.1.1 Debye dielectrics

Debye materials can be thought of as a simple RC circuit where the amount of polarization is related to the voltage across the capacitor [69]. The basic first-order dielectric response was found by Debye in 1926. For a dielectric material. Debye's equation is [70]:

$$\epsilon_r(s) = \epsilon_\infty + \frac{\epsilon_s - \epsilon_\infty}{1 + s\tau_e} \tag{3.1}$$

In Eq. 3.1, ϵ_∞ is the optical relative permitivity, ϵ_s is the static relative permitivity and τ_s is the electrical relaxation time. In the Fourier domain (s $\rightarrow jw$) this function splits into real (ϵ_r') and imaginary (ϵ_r'') parts as:

$$\epsilon_r(w) = \left(\epsilon_\infty + \frac{\epsilon_s - \epsilon_\infty}{1 + w^2\tau_e^2}\right) - j\left(\frac{(\epsilon_s - \epsilon_\infty)w\tau_e}{1 + w^2\tau_e^2}\right) \tag{3.2}$$

which is often written in the form:

$$\epsilon_r(w) = \epsilon_r'(w) - j\epsilon_r''(w) \tag{3.3}$$

Physically, ϵ_r' describes dispersion and ϵ_r'' absorption phenomena respectively.

3.1.1.1 Tissue characteristics

The famous work of Gabriel in [71] presents a compilation of the dielectric properties of body tissues as a function of frequency. This kind of tissues cannot be accurately described with the single relaxation Debye model. From the analysis of Gabriel's data, the measured relative permitivity ϵ_r of biological media can be described over the range 1 MHz -10 GHz [72].

$$\epsilon_r = \frac{\sigma_e}{s\epsilon_0} + 1 + \chi_e = \frac{\sigma_e}{s\epsilon_0} + \epsilon_\infty + \frac{\chi_{e0}}{1 + s\tau_{e0}} + \frac{\chi}{1 + s\tau_{e1}} \tag{3.4}$$

The aforementioned is used as a reference by Andreuccetti *etal*. in the dielectric properties calculator application available in [73] which is used in this work.

Table 3.1 presents the parameters of the extended Debye model for bone and brain tissue.

Table 3.1: Dielectric parameters of bone and brain tissue [74, 75].

Tissue type	ϵ_∞	χ_{e0}	τ_{e0} $[ns]$	χ_{e1}	τ_{e1} $[ps]$	σ_e [Sm^{-}1]
Cortical Bone	5	25	5	7.5	20	0.03
Cancellous Bone	6	65	5	14	20	0.09
Average Bone	5.5	45	5	10.8	20	0.06
White Matter	18	130	5	20	15	0.13
Grey Matter	20	250	4	32	15	0.23
Average Brain	19	190	4.5	26	15	0.18

Fig. 3.1 illustrates the conductivity and relative permitivity of several relevant tissues as a function of frequency. We can see that all of them have a similar behavior perhaps with the exception of dry skin at low frequencies. For a frequency range of 1 kHz to 10 GHz, the conductivity varies from 0.01 to 10 [S/m] and the relative permitivity from 40000 to 10 [F/m] respectively. The permeability of biological tissue is considered to be the same as the free space ($\mu_r = 1$).

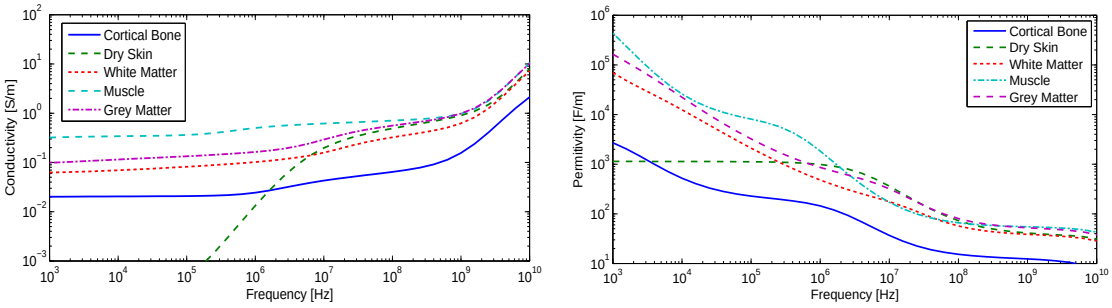

(a) Conductivity.

(b) Permitivity.

Figure 3.1: Tissue properties as a function of frequency.

3.2 Specific Absorption Rate

The magnetic energy absorbed in the near field of a transmitter can be given by [68, 76]:

$$SAR_H = \frac{\sigma}{\rho}\frac{\mu w}{\sqrt{\sigma^2 + \epsilon^2 w}}\left(1 + \delta_{corr}\Gamma\right)^2 H_{rms}^2 \tag{3.5}$$

where ρ is the tissue density and Γ is the reflection coefficient of a plane wave in the tissue defined as:

$$\Gamma = \frac{2\left|\sqrt{\epsilon_\Gamma}\right|}{\left|\sqrt{\epsilon_\Gamma} + \sqrt{\epsilon_0}\right|} - 1 \tag{3.6}$$

In this expression, ϵ_Γ corresponds to the complex permitivity $\epsilon_\Gamma = \epsilon - \sigma/jw$. The term δ_{corr} is a correction term accounting for the distance in between the transmitter and tissue obtained empirically by Kuster and Balzano in [76]:

$$d_{corr} = \begin{cases} 1, & d \geq 0.08\lambda/\Gamma \\ sin\left(\frac{\pi|\Gamma|d}{2\times 0.08\lambda}\right), & d < 0.08\lambda/\Gamma \end{cases} \tag{3.7}$$

For the case of a single circular loop carrying an alternate current, the magnetic at a distance d from the coil is:

$$H = \frac{I_1 r_1^2}{2\left(\sqrt{r_1^2 + d^2}\right)^3} \tag{3.8}$$

Thus , the collected field of a receiver with a radius r_2 is:

$$H_r = \frac{I_1 r_1^2 \pi r_2^2}{2\left(\sqrt{r_1^2 + d^2}\right)^3} \tag{3.9}$$

Substituting Eq. (3.9) in (3.5) we obtain:

$$SAR_H = \frac{\sigma}{\rho}\frac{\mu w}{\sqrt{\sigma^2+\epsilon^2 w}}(1+\delta_{corr}\Gamma)\frac{1}{2}\left[\frac{I_1 r_2^2 \pi r_2^2}{2\left(\sqrt{r_1^2+d^2}\right)^3}\right]^2 \tag{3.10}$$

In order to be able to quantitatively compare the level of absorption by both the magnetic and electric fields, we can compare them at the near-field edge where E-field propagation takes over from H-field coupling relying on the expression of the SAR induced by the E-field presented in [68]:

$$SAR_E = \frac{\sigma\beta^2\eta^2}{\rho}\frac{I^2 l^2 sin^2(\theta)}{(4\pi d^2)^2} \tag{3.11}$$

The ratio of the absorption rates in the near field edge where $d = \lambda/2\pi$, $\beta = 2\pi/\lambda$, $\mu_r = 1$, $\eta = \sqrt{\mu_r\mu_0/\epsilon_r\epsilon_0}$ and $Z_0 = \sqrt{\mu_0/\epsilon_0}$ is [68]:

$$\frac{SAR_H}{SAR_E} = \frac{Z_0^2}{\eta^2}\frac{1}{\sqrt{\epsilon_r+(\sigma^2/\epsilon_0^2 w)}} = \frac{\epsilon_r}{\sqrt{\epsilon_r+(\sigma^2/\epsilon_0^2 w^2)}} \tag{3.12}$$

By using Eq. 3.12 and the tissue parameters obtained from [73] and presented in Fig. 3.1, we can plot the ratio of magnetically induced and electrically induced SAR with respect to frequency, as presented in Fig. 3.2.

3.3 Summary

In this chapter we have introduced the frequency response of biological tissue and analyzed the specific absorption rate of both E and H-fields. Based on definitions available in literature, we determined the SAR ratio of magnetic and electric fields for the relevant tissues in our application as a function of frequency, using the frequency dependent dielectric parameters of tissues. We found that in the low MHz range the H-field SAR accounts for less that 10 % of the E-field SAR. Thus, we can conclude that in this frequency range, a near field inductive link leads to smaller absorption of coupled energy in tissues. At

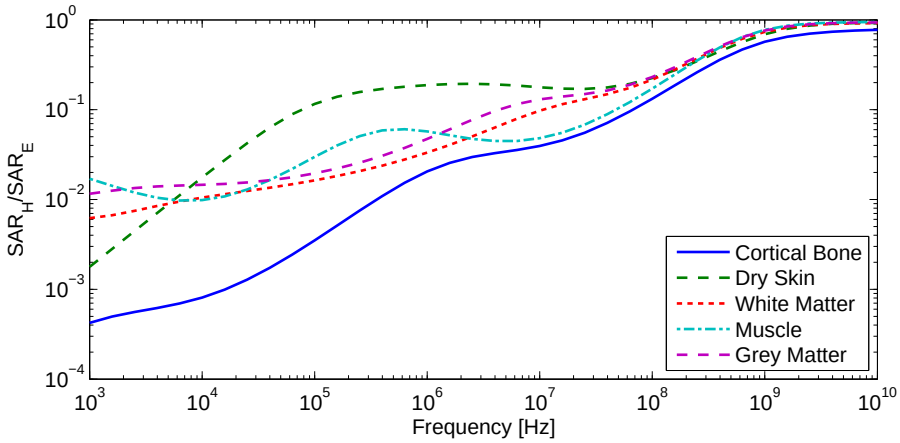

Figure 3.2: Ratio between H-field and E-field induced SAR.

higher frequencies, the difference is not so pronounced and other factors must also be taken into account when selecting appropriate operating approach.

Chapter 4

Circuit Design

After having studied and understood the inductively coupled interfaces and biological body area network channels, the circuit level design can be addressed. In this chapter we present some design considerations and each of the building blocks of the system at circuit level.

4.1 Technology

The technology used for the circuit design is AMS 0.18 μm HV CMOS. The modules provided in this kit include low voltage transistors as well as several modules of high voltage, isolated and thin oxide transistors (5.5, 20 and 50 V). Furthermore, AMS 0.18 μm kit offers additional devices such as MIM[1] capacitors, a broad range of resistors and diodes and high voltage BJT transistors. The technology selection is made in line with the current developments within the Biomedical Electronics Group of Delft University of Technology. Currently, some implantable devices are being designed in this technology and since the energy harvester presented in this work is expected to be part of these systems, the same technology is selected. For this design, the 1.8 and 5.5 V modules are

[1] Acronym for Metal-Insulator-Metal.

used due to the voltage requirements of the power delivery unit (4.2 V). Table 4.1 shows the important transistor parameters for each one of these modules.

Table 4.1: Electrical parameters in the AMS 0.18 μm technology.

1.8 V							
Parameter	**NFET**			**PFET**			**Unit**
	Min	**Nom**	**Max**	**Min**	**Nom**	**Max**	
Threshold voltage (sat)	0.36	0.43	0.5	-0.29	-0.365	-0.44	V
Threshold voltage (lin)	0.45	0.51	0.57	-0.39	-0.45	-0.51	V
Body factor	145	175	205	-190	-215	-240	mV
Gain factor	246	274	305	52	56	59	$\frac{\mu A}{V^2}$
5.5 V							
Threshold voltage (sat)	0.45	0.525	0.68	-0.585	-0.65	-0.715	V
Threshold voltage (lin)	0.55	0.61	0.67	-	-	-	V
Body factor	215	245	275	-220	-250	-280	mV
Gain factor	121	130	139	27	28.5	30	$\frac{\mu A}{V^2}$

4.2 Design Considerations

Prior to the design task, it is important to establish certain criteria and expected conditions of the system based on the intended application. Naturally, it is intended to obtain a design that offers high efficiency at very low input power and that is robust to changes in the operating environment and semiconductor process variations. The robustness of the design will be evaluated by means of circuit simulations based on the technology corners.

Efficiency however, is a concept that must be addressed carefully. For instance, in the transmitter part, the concept of efficiency applies to the DC to RF conversion. For the inductive link, the efficiency inevitably will be a function of the distance and alignment between the coils and the focus should be placed then in increasing the sensitivity of the receiver while maintaing its flexibility to adapt to varying coupling factors. At the receiver side, two major components influence the efficiency; the rectifier and the power delivery circuit. It is important to consider each of them when designing the other to obtain a high performance circuit.

As starting point, we first consider the temperature range of operation. Designed to be implanted inside a human body, the energy harvester will have a very limited temperature range in which it will operate. The body itself will

act as a thermal regulator and therefore temperature aware design is not a critical factor in this application.

Finally, the system's load, which in this case is assumed to be a Li-Ion battery, will determine a number of performance specifications for the power delivery circuit. The following section addresses these kind of batteries in greater detail.

4.3 Li-Ion Batteries

In medical applications, specially those related to implantable devices, Li-Ion batteries are the preferred technology for energy storage. The high nominal voltage allows for one Li-Ion cell to be used in place of three Ni-Cd or three Ni-M hybride cells [77]. This, in conjunction with their higher energy densities and low self-discharge rates bring major advantages such as ease of implantation and lifetime. Fig. 4.1 shows the discharge curve for a 1 Ah Li-Ion battery. Although the nominal voltage of this kind of cells is 3.6 V (region shaded in gray), the full charge voltage is 4.2. This is of particular importance for the design of the power delivery circuit, since the true stored capacity of Li-Ion cell is very sensitive to undercharging.

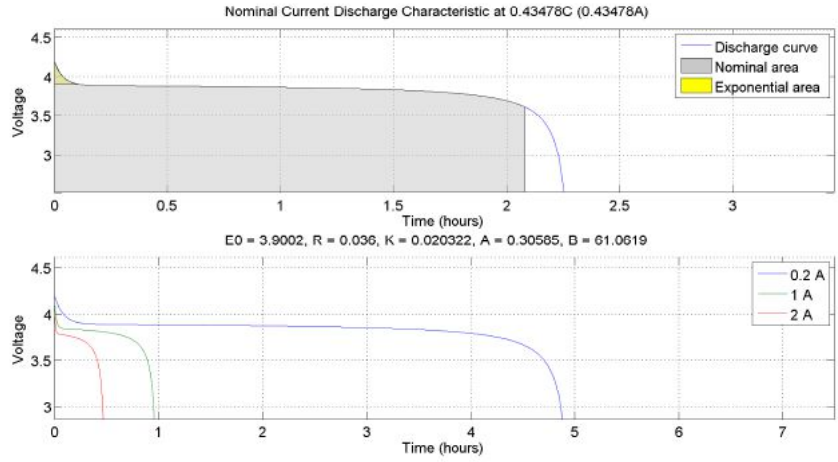

Figure 4.1: Discharging behavior of a 1A-h Li-Ion battery for different load currents.

Fig 4.2 presents the capacity loss versus the percentage of voltage undercharge. Charging to an end-of-charge (EoC) voltage of only 1% less than the full charge

voltage has a great impact on the available capacity of the battery, reducing it almost 8%. However, in order to prevent damaging the cell with overvoltage, the designed EoC voltage has to be a slightly lower value. Since the full charge voltage of these cells changes ± 1% due to process variations and aging, higher accuracy cannot be guaranteed [78]. Thus, the target EoC voltage in the power delivery circuit is defined as 4.15 V.

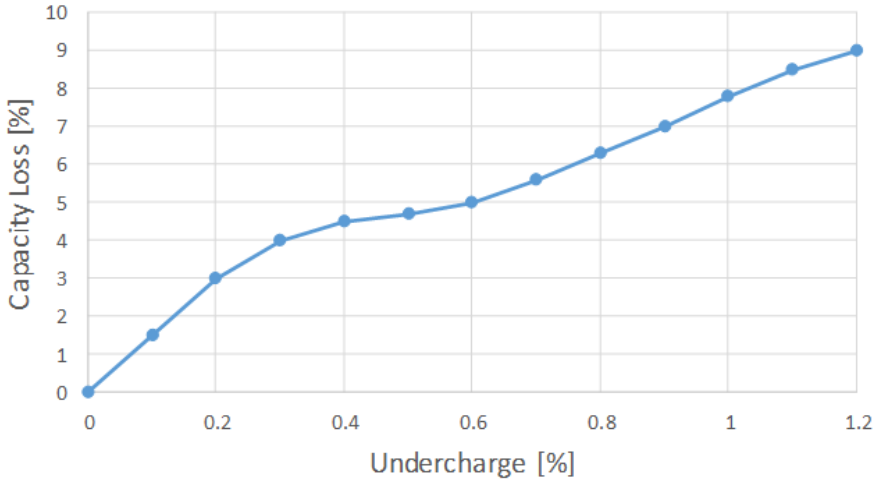

Figure 4.2: Undercharge vs. Capacity loss

Batteries require a certain algorithm that allows fast charging in a safe fashion. For Li-Ion, the most popular algorithm used is the *constant current - constant voltage* (CC-CV) algorithm with an initial trickle charge stage if the cell is heavily depleted. The initial charging current during the CC stage ranges between 0.7 and 1 C, where C is the rated capacity of the battery in Ampere-hour. For instance, a 100 mA-h battery that is charged at a 0.7 C rate receives 70 mA of current until the CV stage of the algorithm kicks in, typically when the battery has reached the EoC voltage. Fig. 4.3 shows the cell voltage, charging current and SoC of a Li-Ion battery when charged using the CC-CV algorithm. Nevertheless, if the available input power is not enough to reach such high current values, the CC-CV algorithm is no longer necessary, as it is in fact the case of our intended application. When the charge rate during the CC phase is low, the charging process will spend less time during the CV tail. If the battery is charged below 0.18 C, only the CC stage can be used and the EoC is then triggered when the target voltage is reached [79].

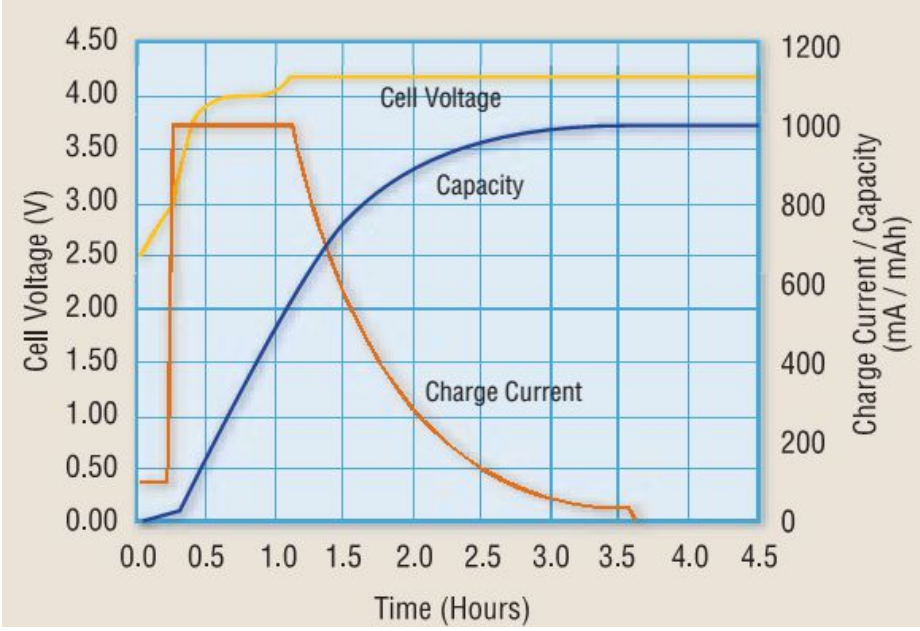

Figure 4.3: Charging of a Li-Ion cell using the CC-CV algorithm. Courtesy of [78].

4.4 Transmitter

The transmitter is a very important part of any WPT system as it is a deciding factor of the efficiency of the entire link. When near-field resonant inductive links are concerned, the transmitter cannot be designed as a standalone subsystem loaded by a standard 50 Ω termination but has to be designed consistently with the magnetic resonant circuit which at the same time settles on the oscillator frequency and represents its actual load. This allows to simultaneously ensure the oscillation condition and the highest conversion efficiency for any possible working state

Typical wireless sensor networks operate at the UHF bands. In order to improve overall transmitter efficiency, power oscillators and injection locking schemes have been reported using conventional a class-E PA [54]. Excellent results for medium power link operating in the 400 MHz band are demonstrated by the design of a class-E oscillator making use of harmonic-balance techniques [80, 81]. The optimum operating point, for the highest conversion efficiency, is obtained after the design of the reactive network. For this reason these solutions are certainly appropriate when the oscillator load is known and is not expected to change significantly. In case the resonator's distance is not fixed

or if the coil alignment is not guaranteed, the coupling factor influences their resonant frequency and hence the oscillator is required to be tuned accordingly. A topology that address this situation is presented in 4.4.

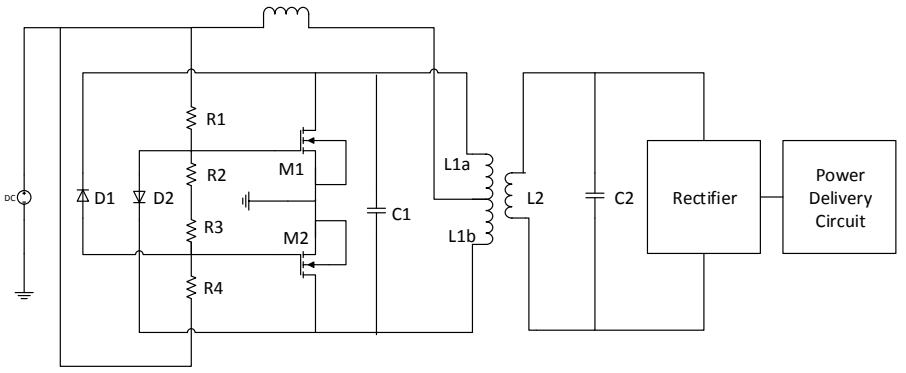

Figure 4.4: Circuit schematic of a WPT driven by a Royer type Oscillator.

The oscillator consists of two cross-coupled MOSFETs connected to a resonant circuit (transmitter) formed by the center-tapped inductor L_{1a-b} and the capacitor C_1. This resonator acts as the primary side link coil of the power system and is coupled to a secondary resonant circuit (receiver) formed by L_2 and C_2, which is connected to a rectifier and the power delivery unit. Due to circuit symmetry, either one of the switches is in the *on* state and forces the control voltage of the other one to zero, setting it to the *off* state [54].

If the transmitter resonator is weakly coupled to the receiver, its angular resonant frequency is given by:

$$\omega_0 = \frac{1}{\sqrt{2(1+k)LC_1}} \tag{4.1}$$

where L corresponds to the common value of inductance of the two sections of L_1 and k is their coupling factor. If the loaded Q factor of this resonant circuit is high enough, one can assume that the voltage across C_1 is a sinusoidal wave:

$$V_{C_1} = V_M sin(\omega_0 t) \tag{4.2}$$

Supposing that initially the transistor M_1 is *off* and M_2 is *on* during the first half of the period of V_{C_1}, the drain voltage of M_1 is ideally equal to V_{C_1} and

positive, keeping the transistor M_2 in the *on* state. Consequently, the voltage drop across M_2 is (ideally) zero and M_1 remains *off*. At $t = \pi/\omega_0$, V_{C_1} equals zero and M_2 is turned *off*, increasing its drain voltage. This allows M_1 to turn *on* for the second half of the period of V_{C_1} while its drain voltage is kept zero. This situation is maintained until $t = 2\pi/\omega_0$ when the cycle restarts.

The value of the inductance L_{choke} is chosen such that its impedance is large at the resonance frequency, making the RF current to circulate only through the loop formed by L_1 and C_1. The DC voltage source and L_{choke} behave as a DC current source. A DC current is injected to the central tap of L_1 and only flows through the switch that is in the *on* state.

The amplitude voltage of the central tap of L_1 can be expressed as:

$$V_{L_{1b}}(t) = -V_{L_{1a}}(t) = \frac{V_M}{2} sin(\omega_0 t) \tag{4.3}$$

where V_M is the amplitude of the resonator voltage. It follows then that the voltage of the central tap of L_1 is a rectified sinusoid of amplitude $V_M/2$, whose average value is given by:

$$V_{AV.} = \frac{\omega_0}{\pi} \int_0^{\frac{\pi}{\omega_0}} \frac{V_M}{2} sin(\omega_0 t) dt = \frac{V_M}{\pi} \tag{4.4}$$

Given that the DC component of the voltage across L_{choke} is zero, V_{AV} must then be equal to the DC source voltage. Thus, one can determine the relation between the resonator amplitude and the DC source to be:

$$V_M = \pi V_{DC} \tag{4.5}$$

The induced voltage V_{IND} at the receiver side depends on the quality factor Q_{Rx} of the receiver resonator and the coupling factor k. If the receiver is unloaded, one can express V_{IND} as:

$$V_{IND} = k Q_{Rx} \sqrt{\frac{L_2}{L_1}} \tag{4.6}$$

For a given coil and capacitor parasitic resistances, there exist an optimal LC

combination that provides the highest quality factor possible. The inductance value is constrained by the feasibility of coil implantation whereas the capacitance value offers more flexibility. This problem can be expressed as an optimization problem with linear and non-linear constraints in the following form:

Maximize

$$Q_{Rx}$$

subject to:

$$L_{Rx} \leq L_{max}$$
$$\omega_0 = \frac{1}{\sqrt{L_{Rx} C_{Rx}}}$$

Where

$$Q_{Rx} = Q_{Lx} || Q_{Cx}$$
$$Q_{Lx} = \frac{\omega_0 L_{Rx}}{R_{L_{Rx}}}$$
$$Q_{Cx} = \frac{1}{\omega_0 C_{Rx} R_{C_{Rx}}}$$

For this design, the value of L_{max} is set to 1 μH extracted from the maximum achievable inductance value of the receiver coil and ω_0 is set to $2\pi \times$ 6.78 Mrad/s. Although there exist certain flexibility, the selection of this frequency is made such that the system operates inside one of the available ISM[2] bands. For the sake of simplicity, the ω_0 used in the optimization routine uses the theoretical definition and not that of Eq. 4.1 for weakly coupled inductors. Since the coupling factor is small and impossible to predict at any given time, this approach introduces very little error in the component's calculation. This problem is solved using the *fmincon* tool in the MATLAB environment. The values of the parasitic resistances of C and L are taken from *COTS* components

[2]Industrial, Scientifical and Medical.

and wire resistance calculators available on most manufacturer's website.

In [62, 82], the system coupling uses identical primary and secondary resonators. Despite that, it is important to notice that eventually, it is possible to design the transmitter and receiver resonators with different component values since the transmitter side is not as tightly constrained as the receiver side and thus its design space can be extended. At first, one may think that by using a high turns ratio N_{Rx}/N_{Tx} for the coils, it is possible to induce a much higher voltage. This is not necessarily the case as the mutual inductance and the quality factors also get affected with this change, showing a clear trade-off to be addressed. Table 4.2 presents the component values and input voltage utilized in the design of the resonator.

Table 4.2: Component values used in the transmitter design.

Transmitter	
V_{DC}	1.8 V
$D_{1,2}$	CMDSH2-3
$R_{1,4}$	100 Ω
$R_{2,3}$	100 kΩ
L_{choke}	100 μH
C_1	7 nF
$L_{1a,b}$	39 nH
$M_{1,2}$	W=30 mm L=700 nm
Receiver	
C_2	0.7 nF
L_2	780 nH

For the transmitter, Fig. 4.5 shows the drain-source voltage and drain current through the switches during the oscillation condition. Although this configuration operates with ZVS/ZCS[3] (which enhances the overall RF to DC efficiency); due to the finite R_{ON} resistance and parasitic capacitances, the power dissipation in the switches arises as the greatest source of losses. In practical implementations, the conversion efficiencies can easily reach more than 80% [54].

Fig. **??** shows the behavior of the oscillation frequency as a function of the coupling factor. Both the x and y-axis represent the oscillation frequency. It is seen that for low values of k, the oscillation frequency remains close to f=$\omega_0/2\pi$ whereas for high values of k, the resonant frequency exhibits two maximum located at $f_1=\omega_0/(2\pi\sqrt{1+k})$ and $f_2=\omega_0/(2\pi\sqrt{1-k})$, with very little power

[3] Acronyms for Zero Voltage Switching and Zero Current Switching.

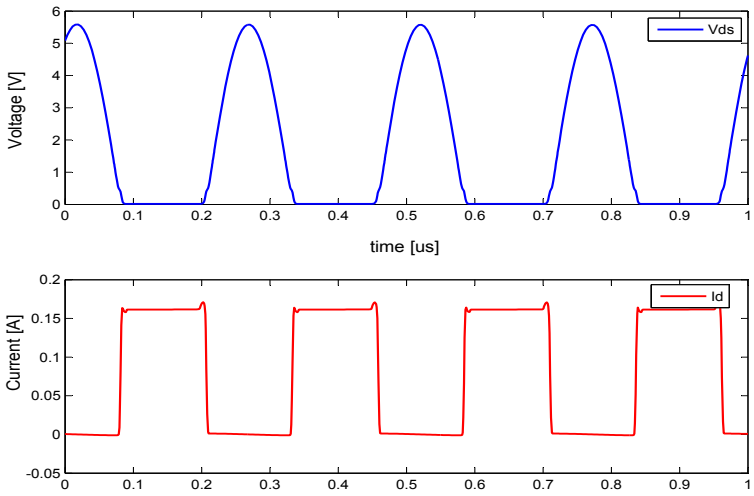

Figure 4.5: Switch drain-source voltage and drain current.

exchange occuring at the original designer oscillation frequency. Furthermore, according to [82], the peak located at lower frequency provides higher values of output power.

4.5 Rectifier

Once the the incoming RF power reaches the receiver side, it is necessary to convert it back into DC to feed it into our storage element. To achieve this, first the RF signal must be rectified and then processed to meet the requirements of the Li-Ion battery (*i.e.* shift the voltage to the appropriate level).

In standard CMOS processes, the diodes are commonly replaced with the diode-tied MOS transistors that are easier to implement [83]. However, in such configurations, the circuit is still affected by the threshold voltage, which, added to the instantaneous drain-source voltage drop results in degraded power efficiency and lower voltage drop. Another option is the usage of Schottky diodes with low forward drop is possible, but their implementation is expensive due to the extra processing steps required, unavailable in standard CMOS technologies [84].

Full-wave bridge rectifiers (FWBR) are a popular version of the full-wave rectifiers. They offer high power efficiencies, smaller output ripples and greater reverse breakdowns when compared with the half-wave rectifiers [85].

For this project, we have chosen the full-wave fully gate cross-coupled rectifier topology, shown in Fig. 4.6. This circuit solves the problem of the extra threshold voltage drop across the PMOS transistors of the conventional bridge full-wave rectifier. The drawback is lower power efficiency due to the flow-back current from the output node. The selection is made based on the trade-off existing between operating range and efficiency. By using the fully gate cross-coupled topology of Fig. 4.6 we are able to operate the circuit at lower voltages, which corresponds to a larger coil separation or misalignment. Furthermore, studying the load of the rectifier (the power delivery unit) allows us to determine its impact on the system's performance.

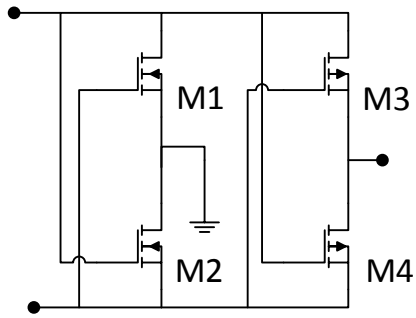

Figure 4.6: Full-wave cross-coupled rectifier.

Although there is a possibility of using a multi-stage rectifier, the approach chosen here favors the usage a single stage only, leaving the the step-up task to the latter power delivery unit. This is done because in the worst case scenario (low input voltage and battery almost fully charged), we would need at least 6 rectifying stages, severely affecting efficiency. Ideally, a voltage-to-voltage transfer such as the one that a boost converter provides would give us the required step-up voltage with 100 % efficiency. Moreover, due to its controlled nature, it is possible to effectively block any flow-back current, avoiding the discharge of the battery.

Defining the power conversion efficiency of the rectifier as:

$$PCE = \frac{P_L}{P_R} \tag{4.7}$$

where P_L is the average output power at the load and P_R is the average real input power at the rectifier's input; it is clear that, in order to size the rectifier properly, we need to know what the values of P_L and P_R are. Since we have established that the distance of the coils can vary, so can P_R. For this reason, the average input power must be selected based on the "most common" operating condition, which of course will depend on the physical design of the link.

Recalling the findings of Ch. 2, for a distance variation of 1 to 10 cm we can expect coupling factors between 0.04 to 0.004, assuming the transmitter being 5X bigger than the receiver. If we arbitrarily choose 0.01 as the "most common", it is possible to extract P_R from the previously designed transmitter. As of P_L, we encounter a similar situation. In steady state, the average load power will depend on the power delivery unit and lastly, on the Li-Ion battery itself. Considering the common state of the battery as being halfway depleted (say it is at its nominal voltage of 3.6 V), only the charging current is needed to establish the average power.

4.6 Boost converter

4.6.1 Fundamental model

Fig. 4.7 represents the typical structure of a synchronous boost converter circuit. This circuit has the ability to provide a voltage V higher than its input voltage Vg. The synchronous approach is preferred over the asynchronous since the forward voltage drop across the diode used in the latter has a detrimental impact in the circuit's efficiency.

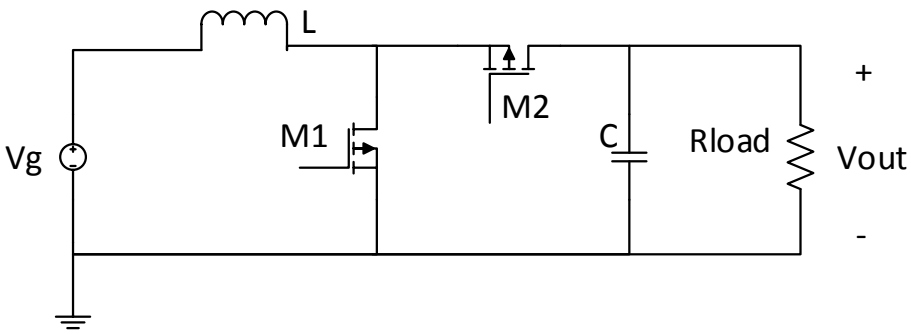

Figure 4.7: Basic schematic of a boost converter.

Assuming ideal components, the principle of operation can be illustrated using the equivalent circuit in Fig. 4.8. Transistors M_1 and M_2 work as switches with opposite phase. When the transistor M_1 is switched on (M_2 off), the right-hand side of the inductor is effectively connected to ground. Using the volt-second balance and charge balance principles as well as the small ripple approximation, the inductor voltage and capacitor current can be expressed as in (4.8).

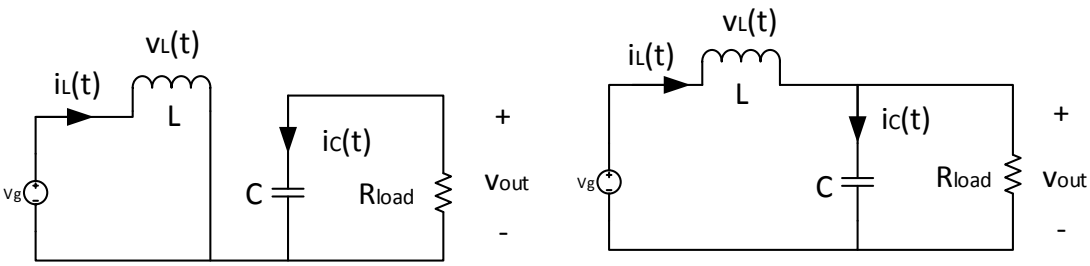

(a) Inductor charging.

(b) Inductor discharging.

Figure 4.8: Operating states of an ideal boost converter.

$$v_L = Vg \tag{4.8a}$$

$$i_C = -\frac{V_{out}}{R_{load}} \tag{4.8b}$$

With the switch M_1 turned off (M_2 on), the connection looks like in Fig. 4.8(b). The inductor voltage and capacitor current are then:

$$v_L = Vg - V_{out} \tag{4.9a}$$

$$i_C = I - \frac{V_{out}}{R_{load}} \tag{4.9b}$$

The total volt-seconds applied to the inductor over one switching period are:

$$\int_0^{T_s} v_L(t)dt = (V_g)DT_s + (V_g - V_{out})D'T_s \tag{4.10}$$

where D is the duty cycle of the switch M_1 and $D' = 1\text{-}D$. The value of Eq. (4.10) over one switching period in steady-state must equal zero according to the volt-second balance. Hence:

$$V_g(D + D') - VD' = 0 \tag{4.11}$$

which leads to a voltage conversion ratio $M(D)$ given by:

$$M(D) = \frac{V_{out}}{V_g} = \frac{1}{D'} = \frac{1}{1 - D} \tag{4.12}$$

It is important to notice that the results presented in (4.12) are only valid if the current through the inductor L never goes to zero. The converter is then said to be operating in the Continuous Conduction Mode (CCM). Fig. 4.9(a) illustrates an example of the current when in CCM. If the current reaches zero for a finite amount time during each switching period then the converter is said to be operating in Discontinuous Conduction Mode (DCM). Fig 4.9(b) shows the inductor current waveform in such condition. Notice that for DCM, there is an *on* time D_1, *off* time D_2 and *idle* time D_3 during each cycle. For this particular mode of operation, the voltage conversion ratio becomes a function of D_1 and a parameter K and is defined as [86]:

$$M(D_1, K) = \frac{2}{1 + \sqrt{1 + \frac{4K}{D_1^2}}} \quad \text{if} \quad K < K_{crit}(D) \tag{4.13}$$

where,

$$K = \frac{2L}{RT_s} \quad \text{and} \quad K_{crit}(D) = D' \tag{4.14}$$

The dimensionless parameter K is a measure of the tendency of a converter to operate in the discontinuous conduction mode. Large values of K lead to continuous mode of operation, while small values lead to the discontinuous conduction mode for some values of duty cycle [86].

An important characteristic of this converters is that their open loop gain differ depending on its operating regime. Contrary to CCM, where dc-dc converters exhibit two poles and a RHP zero; DCM has only one pole and no RHP zeros,

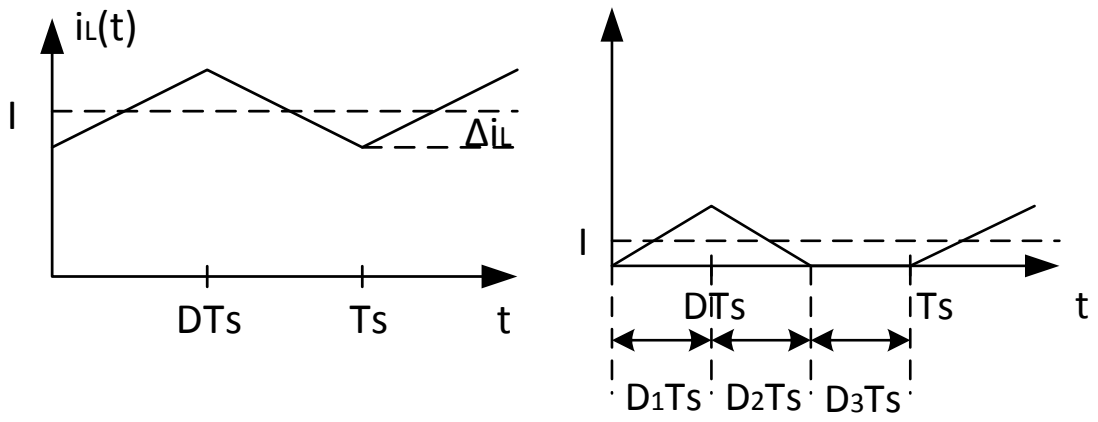

(a) Continuous Conduction Mode (b) Discontinuous Conduction Mode

Figure 4.9: Inductor current comparison

making it unconditionally stable when feedback is applied. This factor makes the usage of systems that fully operate in DCM more attractive, specially for low power applications [87].

4.6.2 Losses

In dc-dc converters, there exist three major loss sources that must be addressed properly in order to maximize efficiency: Conduction losses, switching losses and control losses.

4.6.2.1 Conduction Losses

The conduction losses come from the parasitic resistance that appear in the current path while transferring energy from input to the output. The major contributors here are the R_{ON} of the switches and the ESR[4] in the inductor and filter capacitors. Fig. 4.10 represents the equivalent circuit model of a boost converter including an ideal dc transformer, winding resistance (R_L) and MOSFET losses (R_{S1-2}). The output voltage can be expressed as follows:

[4] Acronym for Equivalent Series Resistance.

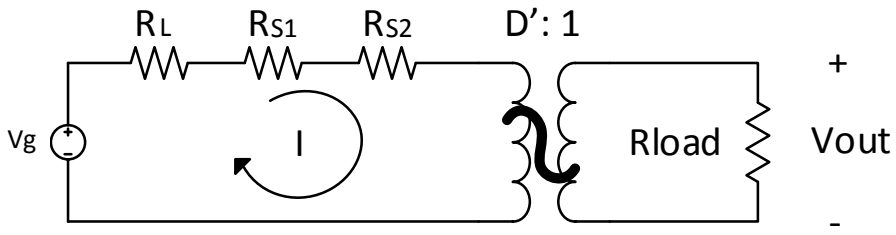

Figure 4.10: Equivalent boost converter including conduction losses.

$$V_{out} = \left(\frac{V_g}{D'}\right)\left(\frac{1}{1+\frac{R_L+DR_{S_1}+D'R_{S_2}}{D'^2R_{load}}}\right) \tag{4.15}$$

Dividing by V_g gives the voltage conversion ratio:

$$\left(\frac{V_{out}}{V_g}\right) = \left(\frac{1}{D'}\right)\left(\frac{1}{1+\frac{R_L+DR_{S1}+D'R_{S2}}{D'^2R_{load}}}\right) \tag{4.16}$$

Eq. 4.16 shows that the impact of the lossy elements is a reduction on the effective voltage conversion ratio from the ideal value ($1/D'$). The efficiency is given as $\eta = P_{OUT}/P_{IN}$. From Fig. 4.10 we know that $P_{IN} = V_g I$ and $P_{OUT} = V_{out} D' I$. Thus, the efficiency can be expressed as in Eq. 4.17.

$$\eta = D'\left(\frac{V_{out}}{V_g}\right) = \frac{1}{1+\frac{R_L+DR_{S1}+D'R_{S2}}{D'^2R_{load}}} \tag{4.17}$$

From here, we can extract that in order to obtain high efficiency, the following condition must be met:

$$D'^2R_{load} >> R_L + DR_{S1} + D'R_{S2} \tag{4.18}$$

As stated by [86], this model correctly predicts the conduction losses in these elements as long as the inductor current ripple is small. In our design, this is not the case, as the BRM condition forces the ripple current $\Delta I = I$. As

a consequence, the rms current through the switches is 1.15 I/$\sqrt{D}$ and the average power loss in R_{ON} equals 1.33 DI^2R_{ON}.

Fig. 4.11 presents the variation of R_{ON} of a 5.5 V NMOS transistor as a function of the width, for different driving voltages. The upper boundary is set as if the switches were driven by the minimum input voltage (i.e. the output of the rectifier) and the lower boundary is set if they were driven by the battery's nominal voltage (3.6 V).

There is at least one order of magnitude difference in the resistance between the two boundaries for the entire range of widths. This clearly shows the convenience of connecting the driving elements at the output of the boost converter for the reduction of the conduction losses. However, charging the drivers to a higher voltage also increases switching losses, so care must be taken when following this approach. In addition, the system must be able to start-up regardless of the amount of stored energy at the output node. For this reason, it is convenient to keep the driving connected to the output of the rectifier and, once the system has fully started, switch the drivers to the output node for as long as there is energy to transfer. As expected, larger widths will help in reducing R_{ON}. The price to pay is larger capacitance that will also be a major contributor in the switching losses.

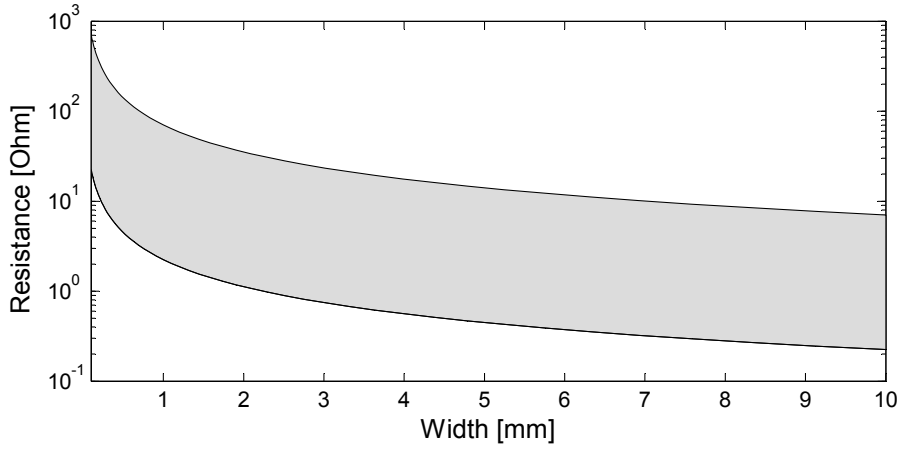

Figure 4.11: Width vs. switches R_{ON} at different drive voltages.

4.6.2.2 Switching losses

Semiconductor devices are charge controlled. For instance, the conduction state of a MOSFET is determined by the charge on its gate and in its channel, and the conducting state of a silicon diode or a BJT is determined by the presence or absence of stored minority charge in the vicinity of the semiconductor junctions inside the device [86]. The process of switching on and off these devices takes a finite amount of time and during this time, significant losses can arise.

Fig. 4.12(a) illustrates the current and voltage waveforms in the switching transistor M. For analysis purposes, the conduction losses are neglected. Ideally, there is no voltage drop in the switch while it is conducting. Similarly, there is not current through the switch if it has been switched off. If M_2 behaves as an ideal diode[5] however, the inductor and M_2 form a clampled load to the transistor that does not allow the transistor voltage and current to change simultaneously. A zoomed-in version of the transition point is shown in 4.12(b). Here we can observe the transistor and diode waveforms as well as the dissipated power after the switching transition. For simplicity, these waveforms are assumed to be piece-wise linear and the diode is considered ideal.

Since the switching times are very short, the inductor current $i_L(t)$ is practically constant during the whole transition time $t_0 < t < t_2$. No current flows through M_2 when $t < t_1$ (i.e. the diode is reverse biased). Undoubtely, the diode cannot become forward biased while its voltage is negative. Hence, in order for M_2 to conduct, its left-hand side voltage (remember Fig. 4.7) must rise to the output voltage V. The inverval length $\Delta t_1 = (t_1 - t_0)$ corresponds in essence to the time it takes to the driver to charge the gate-to-drain capacitance of M_1.

At $t = t_1$, when $v_{ds}(t) = V_{out}$, M_2 starts conducting. Then, the current through the inductor gradually splits between M_1 and M_2 until it fully commutes. The time $\Delta t_2 = (t_2 - t_1)$ is the time it takes to the driver to discharge the gate-to-source capacitance of M_1.

The instantaneous power dissipated by M_1 (depicted at the bottom of Fig. 4.12(b)) is $p_{M_1} = i_{M_1}(t)v_{M_1}(t)$. The energy lost during the turn-off transition can be expressed as:

$$W_{off} = \frac{1}{2} V I_L (t_2 - t_0) \tag{4.19}$$

[5]The ideal diode assumption will let us analyze the switching losses of M_1 and extend its results to M_2. Of course, the timing in the control also influences the losses, but this will be addressed in the control losses section.

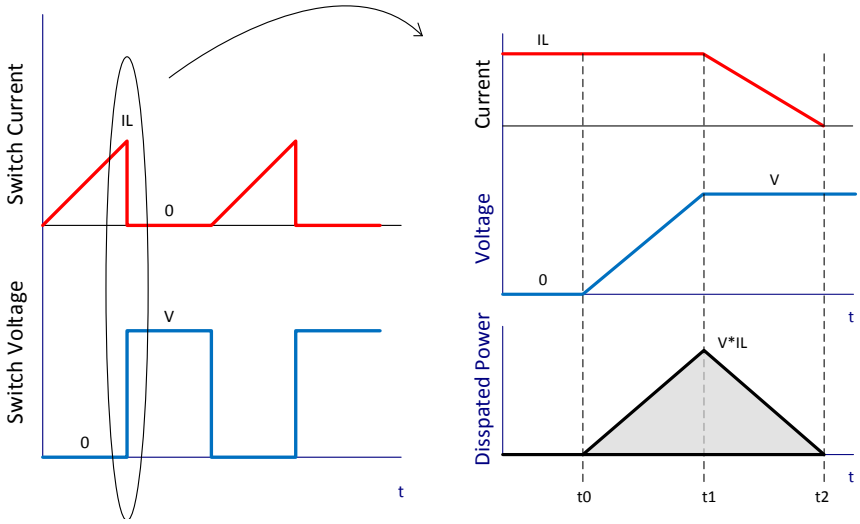

(a) Current and Voltage on the Switch (b) Zoomed-in waveforms

Figure 4.12: *On-Off* transitions in the boost converter switch M_1.

In a similar way, during a turn-on transition, the instantaneous power dissipation has a peak value equal to VI_L and thus the dissipated power on a transition is $\frac{1}{2}VI_L$ times the transition time. If f_s is the switching frequency, the average power loss due to switching corresponds to:

$$P_{sw} = \frac{1}{T_s}\int_{Sw.time} p_{M_1}(t)dt = \left(W_{on} + W_{off}\right) f_s \tag{4.20}$$

From here, one can clearly see that the switching losses are directly proportional to the frequency. Approaches based on PWM techniques (with or without variable frequency) require a certain clock signal to provide the control with a reference to charge/discharge the inductor and transfer the energy to the output. Given that there is a minimum pulse width to be applied at any given period, two situations may arise: The switching is applied sub-optimally and overvoltage can occur at very light load or no load condition.

In addition to the aforementioned, switching losses can also arise as a consequence of the dissipation of the energy stored in parasitic capacitances. If these capacitances are in parallel with switching elements; they are effectively shorted out when the switch turns on, and the energy stored in the capacitance is lost. These capacitances are charged without energy loss when the switching

elements turn off and may even reduce the turn-of losses W_{off}. In a similar way, inductances in series with a switching element lose their stored energy when the switch turns off. Hence, series inductances lead to additional loss at turn-off, but can reduce the transistor turn-on loss [86]. To the extend that capacitors are linear, the stored energy is:

$$W_C = \sum_{Caps} \frac{1}{2} C_i V_i^2 \tag{4.21}$$

Here, the parasitic element that will be responsible for the losses is the drain-to-source capacitance C_{ds}. The C_{ds} value is a strong function of the voltage $v_{ds}$and follows an approximate inverse-square-root dependence of v_{ds} defined as in 4.22 [86].

$$C_{ds}(v_{ds}) = \frac{C_0}{\sqrt{1 + \frac{v_{ds}}{V_0}}} \tag{4.22}$$

With C_0 and V_0 being parameters that depend on the construction of the device. The energy store in C_{ds} at $v_{ds} = V_{DS}$ is:

$$W_{C_{ds}} = \int v_{ds} i_c dt = \int_0^{V_{DS}} v_{ds} C_{ds}(v_{ds}) dv_{ds} \tag{4.23}$$

Where $i_c = C_{ds}(v_{ds}) dv_{ds}/dt$ is the current in C_{ds}. Substituting (4.22) in (4.23) yields.

$$W_{C_{ds}} = \int_0^{V_{DS}} C_0'(v_{ds}) \sqrt{v_{ds}} dv_{ds} = \frac{2}{3} C_{ds}(V_{DS}) V_{DS}^2 \tag{4.24}$$

Fig. 4.13 presents the variation of the equivalent gate capacitance and C_{ds} of the 5.5 V transistors as a function of the width. Both V_{GS} and V_{DS} are kept fixed. With this setup, capacitance increases linearly with the transistor size, ranging between 0.1 and 8 pF approximately. These values can then be used to determine the switching losses due to parasitics and estimate the *critical frequency* of the converter, defined as the frequency where the conduction losses equal the switching losses.

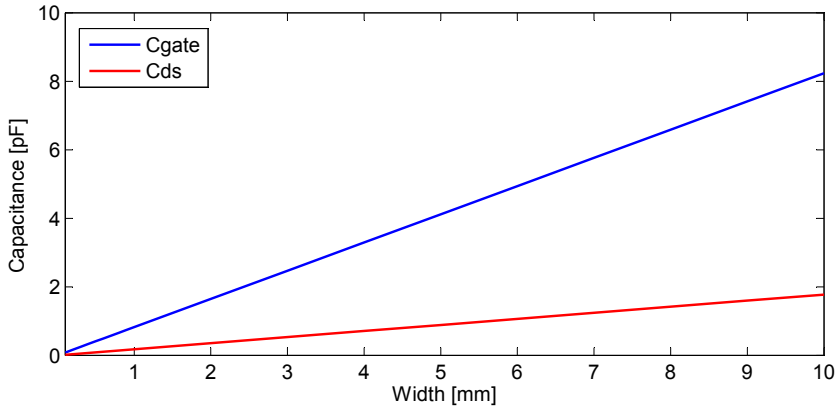

Figure 4.13: Width vs. switches parasitic capacitances C_{gate} and C_{DS}.

4.6.2.3 Control losses

This loss term refers to the losses that the system may incur due to control timing and the power required by the control system in order to make the converter operate properly. The timing issues can be addressed by means of dead time generators that avoid tripping the transistors simultaneously. On the other hand, the power consumed by the control is a power that will not be transferred to the output and therefore it has to be taken into account.

Recalling Eqs. (4.18), (4.20) and (4.24), it is possible to balance the lossy terms to obtain high efficiency. Naturally, it is of our interest to minimize the power consumption of the control. This goal is achieved both by the fully digital control and low power design.

4.7 Proposed approach

The boost converter proposed here is based on the topology presented in [87] and is designed to operate in two different modes, the boundary regulated mode (BRM) and the voltage regulated mode (VRM).

The BRM occurs when the output voltage is less than the target voltage and is attained by ensuring the inductor is fully discharged in each switching cycle.

Provided there is enough power at the input, the BRM exhibits no idle time between charge pulses by operating at the boundary between CCM and DCM. Once the target voltage has been reached, the VRM takes over the control, operating the boost converter in DCM and thus guaranteeing no overvoltage is applied to the load. This approach brings two advantages: First, it completely eliminates the need of a compensation network and second, the switching losses are minimized.

During charging, the inductor current can be expressed as:

$$i_L = \frac{1}{L}\int_{t_0}^{t_1} v_L(t)dt \tag{4.25}$$

For the case that M_1 is an ideal switch, the expression changes to:

$$i_L = \frac{V_{IN}}{L}(t_1 - t_0) \tag{4.26}$$

Ideally, the inductor current increases in a linear fashion and is unbounded when t_1 tends to infinity. However, due to R_{ON}, the maximum current is limited to:

$$i_{L_{max}} = \frac{V_{in}}{R_{ON}} \tag{4.27}$$

If $i_{L_{max}}$ is reached, the power dissipation in the switch equals the input power. Therefore, it is required to define a maximum charging current based on the allowable voltage drop over the switch M_1. If we define this voltage as V_τ we have:

$$I_\tau = \frac{V_\tau}{R_{ON}} \tag{4.28}$$

I_τ equals the peak current during the charging period. If $I_\tau << I_{L_{max}}$ and $t_0 = 0$, the following approximation holds:

$$\frac{V_\tau}{R_{ON}} = \frac{V_{IN}}{L}(t_1) \tag{4.29}$$

Rearranging:

$$\frac{L}{R_{ON}} = \frac{V_{IN}}{V_\tau}(t_1) \tag{4.30}$$

Where L/R_{ON} corresponds to the time constant of the RL circuit that is formed when charging the inductor. The energy losses per switching cycle can be written as:

$$W_\tau = \frac{1}{2} V_\tau I_\tau t_1 \tag{4.31}$$

Similarly, the energy stored in the inductor can be approximated by:

$$W_L = \frac{1}{2} L I_\tau^2 \tag{4.32}$$

Using Eqs. (4.30) and (4.32) it is possible to determine the values of L and R_{ON} (transistor width) for a desired maximum value of conduction losses.

To operate the boost converter in DCM, W_L shall be transferred to the load in every switching cycle. This requires the current to fall back down to zero. Since the current in an inductor cannot change instantaneously; at the transition point, where M_1 (M_2) turns off (turns on), using Eq. (4.26) we can state:

$$i_L = \frac{V_{IN}}{L}(t_1 - t_0) = \frac{V_{IN} - V_{OUT}}{L}(t_2 - t_1) \tag{4.33}$$

where t_2-t_1 is the discharging time. For the sake of simplicity, from now on the charging time will be called t_1 and the discharging time t_2.

If we assume a fixed V_{in}, solving (4.33) for t_2 yields:

$$t_2 = \left| \frac{V_{IN} t_1}{V_{IN} - V_{OUT}} \right| \tag{4.34}$$

Considering that V_{out} increases as the battery is charged and V_{in} - V_{out} is

always negative[6], we see that t_2 reduces for larger V_{out}. From here, we can define the maximum switching frequency as:

$$f_{max} = \frac{1}{t_1 + t_{2min}} \tag{4.35}$$

Hence, the maximum switching frequency of the boost converter occurs at the end of the charging process, when the battery has reached 4.15 V. This factor allows us to estimate the expected switching losses and balance them with the conduction losses.

To control the switching phases, a system that enables the inductor charging until the V_τ is reached and disables it when the current drops to zero is required. Conventional topologies found in literature of power electronics address the CCM-DCM boundary operation by placing a sensing resistor in the inductor path in order to detect when reverse current occurs and toggle the control. This comes at the cost of increased conduction losses and high precision comparators. In an energy harvesting environment, avoiding any extra path resistance is highly advisable. Here, we use a 1:1 transformer to sense the charging inductor voltage and use it as a control signal. This approach has been largely overlooked due to the fact that it requires an extra inductor that may be prohibitive due to size and/or cost constraints. Although these are also important aspects here; for the inductance values required in this application it is possible to find transformers with a good form factor to fit them in the limited space available in the implanted device. Fig. 4.14 shows an illustration of the boost converter including the transformer for inductor voltage sensing. By using this voltage sensing method, we pay no penalty in power consumption of the converter.

4.7.1 Control Logic

4.7.1.1 Simulink Model of the Boost Converter

In order to analyze the dynamic characteristics of the boost converter, a simulink model is built. The model is made considering the major non-idealities that would influence the dynamic behavior of the converter, namely switching and conduction losses as well as variable input and output power.

[6]This is in fact true because the minimum output voltage is 2.7 V (when the battery is fully depleted) and the maximum induced voltage at the receiver never reaches such values for the studied distance range and input power.

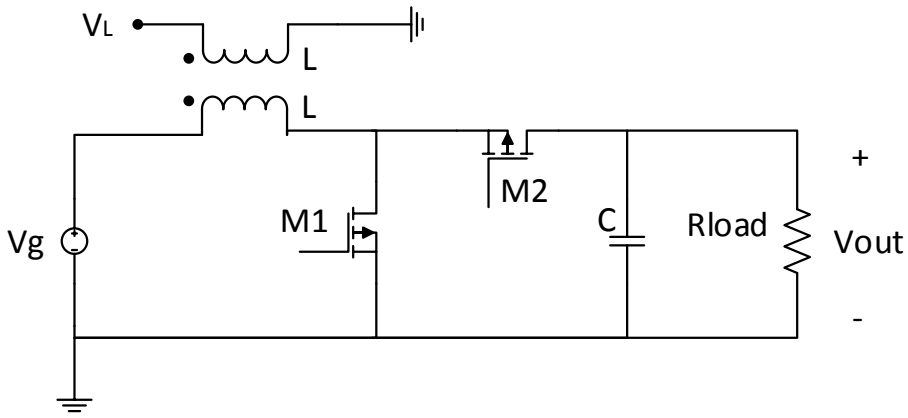

Figure 4.14: Transformer based boost converter for voltage sensing.

Combined with the fundamental knowledge of how this type of circuits operates, the model serves as a solid foundation for the circuit-level design, allowing to study the circuit's performance and extract design guidelines depending on the operating conditions. Fig. 4.15 presents the implemented model using the *SymPowerSystems* toolbox in MATLAB. The model features the aforementioned two modes of operation: BRM and VRM.

The digital control block is implemented as a finite state machine and is presented in Fig. 4.16. Although the control is intended to be completely asynchronous in the circuit implementation; in order to operate properly, the model requires a time reference signal to determine the resolution step in *Simulink*.

This simplified control possesses 4 states. The initial state is used to settle the circuit after any artifact transients that can occur at the beginning of the simulation. In the real implementation, this can represent a state where the input power is not high enough to kickstart the boost converter and hence it remains shut down. After a certain amount of time, if the input voltage is high enough, the control holds in an *idle state*, waiting for the digital input signals to determine the next action. In the *idle* state both M_1 and M_2 are open.

If the output voltage V_{out} is less than V_{TARGET} (4.15 V) minus V_{hyst} (100 mV), the control starts charging the inductor, making M_1 to conduct while M_2 stays open. The converter remains in this state for as long as the voltage across the inductor V_L is greater than a reference voltage V_{REF}. Once V_L falls below V_{REF} the control gives the signal to toggle the switches, discharging

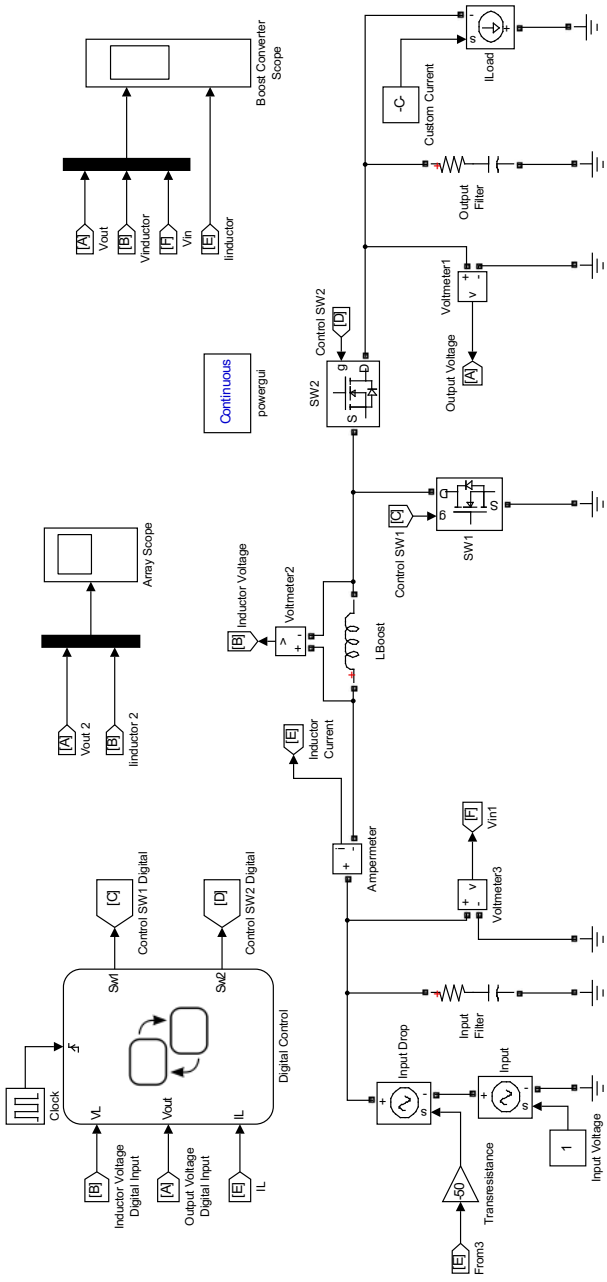

Figure 4.15: Simulink model of the boost converter.

the energy stored in the inductor through M_2 towards the output node. If the current through the inductor falls to zero, all the energy stored in it has been transferred and another charging cycle begins. If $V_{out} > V_{TARGET}$ however, the control sends the system to the *idle* state, ending the charging cycle for as long as the output voltage is higher than V_{TARGET}-V_{hyst}.

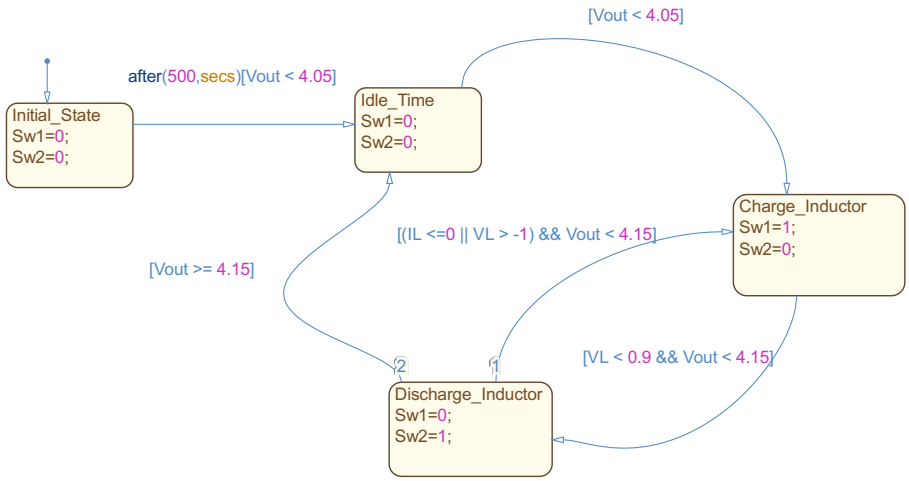

Figure 4.16: Finite State Machine for the boost converter digital control.

Figs. 4.17 presents the behavior of the output voltage and inductor current of the modeled converter with no load and 100 μA load. The figures clearly show the two regimes of operation described before. In Fig. 4.17(b) one can observe that V_{out} takes slightly longer to reach V_{TARGET} due to its load, and the system falls back to Boundary Regulated Mode once more when V_{out} goes under 4.05 V.

In order to determine the zero-crossing point of the inductor current without introducing a sensing resistor in the path, a programmable discharging delay could be implemented relying on Eq. 4.34. The value of t_2 would then be updated for each switching cycle depending on the $V_{IN} - V_{OUT}$ value. Since the output node is loaded with a Li-Ion battery that resembles a huge capacitor, we know the time constant of V_{OUT} is in the order of minutes or hours. Therefore, one could do the update of t_2 every once in a while rather than every cycle. Extending this idea even further, for a certain period of time, one could assume t_2 as a constant. This approach allows the usage of reference voltages to determine the state of the switches in the boost converter. Fig. 4.18 presents the inductor voltage V_L in the *Simulink* model at a certain point in time, where V_{REF1} and V_{REF2} are the reference voltages for comparison

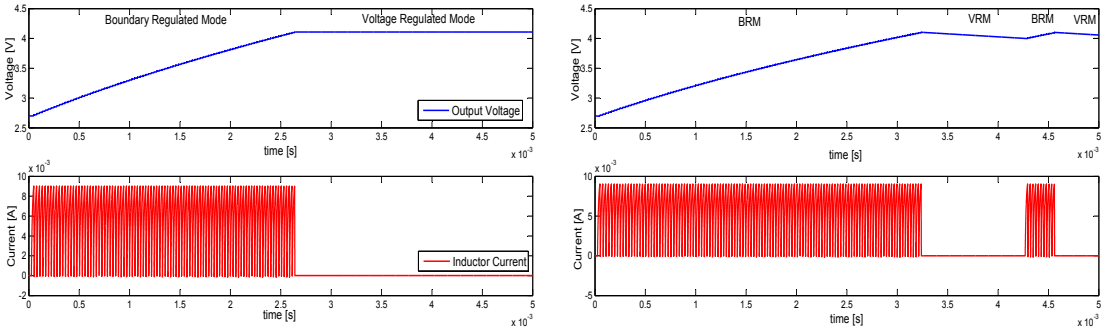

(a) No load.

(b) 100 μA load.

Figure 4.17: Simulink results.

and V_τ the allowable voltage drop in the M_1 switch. Of course, with this approach the zero-crossing point is not accurately defined; but, if we consider the combination of rectifier and DC/DC converter of Fig. 4.19, we see that if there is any flow back current from the output node, it will end up charging C_{rect}. In the next charging cycle when the switches toggle, most of this energy is transferred back to the output node (some of it turns into conduction losses).

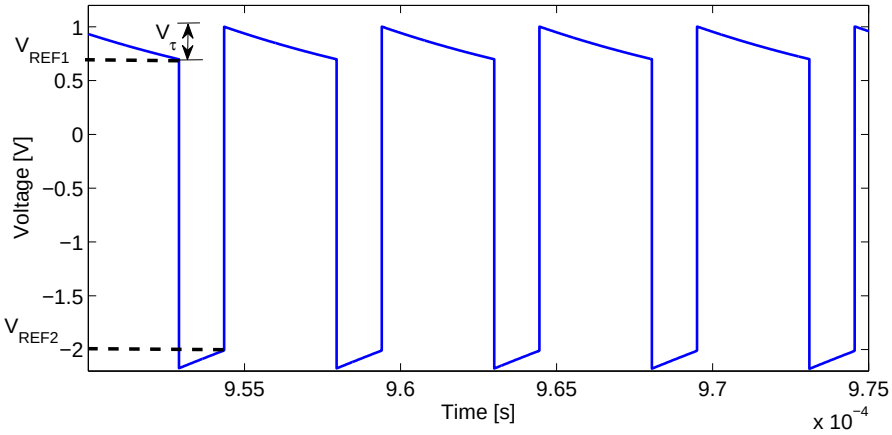

Figure 4.18: Inductor voltage waveform.

The logic function to control the switches could then be defined in the following way:

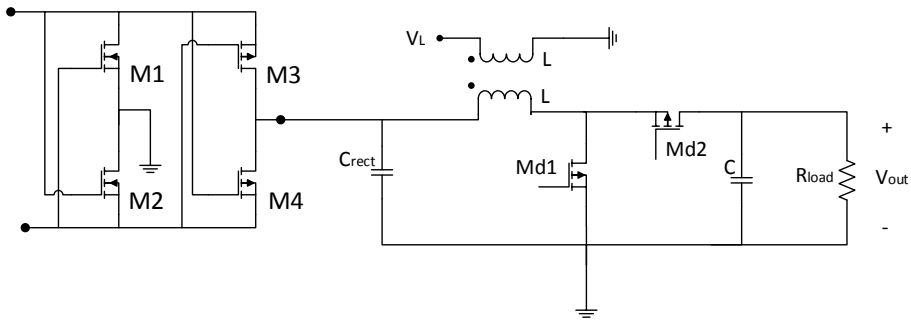

Figure 4.19: Rectifier and boost converter.

- If $V_L > V_{REF1}$, M_1 on and M_2 off (charge inductor).
- If $0 < V_L < V_{REF1}$, M_1 off and M_2 on (discharge inductor).
- If $V_L < V_{REF2}$, M_1 off and M_2 on (discharge inductor).
- If $0 > V_L > V_{REF2}$ M_1 on and M_2 off (charge inductor).

Besides the control presented before, there are other control signals and digital blocks to define in order to be able to fully operate at the circuit level. Fig. 4.20 shows the entire digital control circuit used to operate the boost converter. A voltage adder is used to shift the negative voltage comparison to a zero voltage comparison (V_{ADD} node).

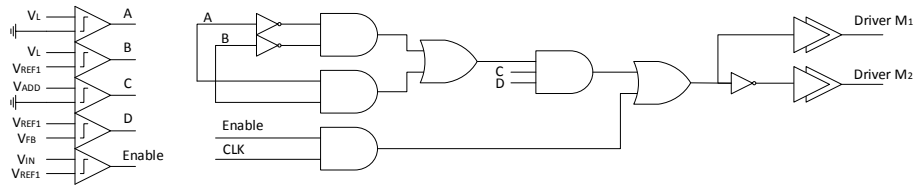

Figure 4.20: Schematic of the complete digital control.

In order for this control system to operate, it is required to have a voltage reference available. Taking into account that this system will be used to charge a Li-Ion battery, the voltage at the output node will never be under 2.7 V. By exploiting this fact, a voltage reference originated at the output node can be used in the energy harvesting system. An enable signal would turn on this reference only when there is enough input power, avoiding any impact in the

lifetime of the battery. Because of this, the design of the voltage reference is left outside of the scope of this work. Despite this, one must remember that a fully autonomous system is possible if a low voltage, low power voltage reference is designed to be powered from the output of the rectifier. For implantable applications, temperature variations would not be of great concern, facilitating the design task. Fig. 4.21 shows the complete system at the circuit level.

4.8 Summary

In this chapter, a detailed presentation of the key components of near field inductive wireless power system has been given. Prior to the circuit analysis, we defined a solid framework in which the circuit would operate, describing the characteristics of the Li-Ion batteries and the technology used. In addition, we have studied at a fundamental level the characteristics of the circuit blocks involved and established a clear design procedure, taking into account our particular application and the existing trade-off between the circuit's performance metrics. Moreover, a new approach in the design of low power DC/DC converter that makes use of the inductor's voltage as a control signal for the digital part is introduced. To support the digital design part and to enhance the understanding of the system, a comprehensive *Simulink* model is developed.

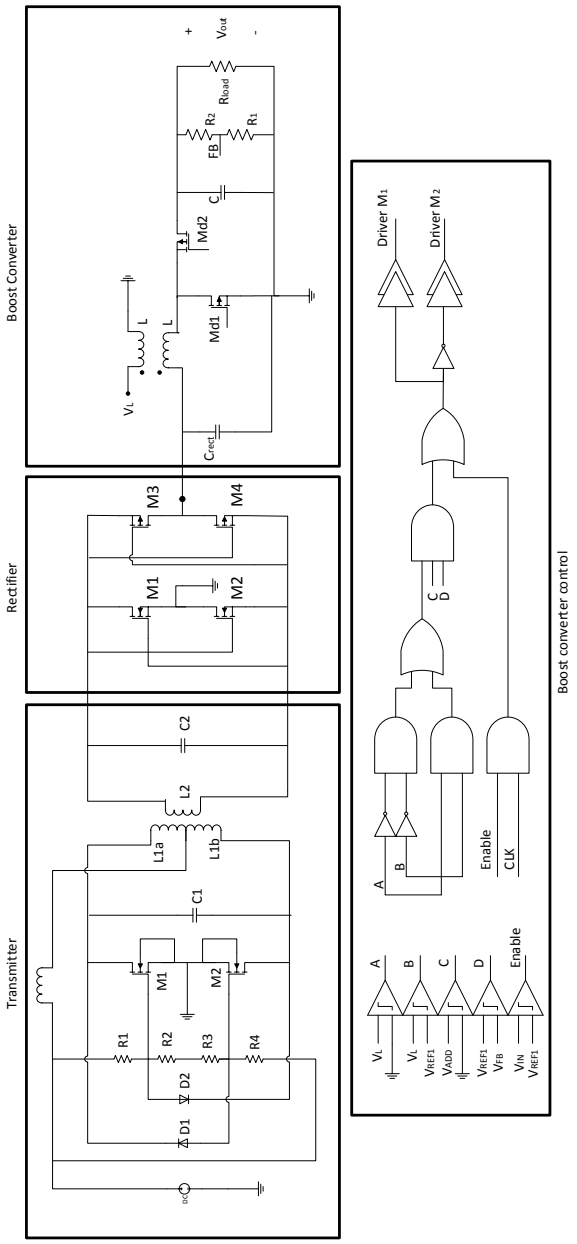

Figure 4.21: Schematic of the entire near field inductive WPT system.

Chapter 5

Simulation Results

This chapter presents the inductive link model validation and simulation results of the circuit designed previously. The building blocks of the system are presented individually and after this, the entire system operation is addressed. Since this device is intended to be used as an implantable device, it is clear that the temperature variations that it will have to endure are minimum[1]. For this reason, a temperature sweep analysis is left aside.

First, we validate the results obtained in the model developed in Ch. 2 by comparing them with those calculated by the ICCDTR[2] tool, available in [] (see Fig. 5.1). Table 5.1 presents the results of this comparison. The data is presented in the form of a ratio $\left(\frac{x_{i,j}}{y_{i,j}}\right)$ where $x_{i,j}$ corresponds to the values extracted from our model and $y_{i,j}$ from the ICCDTR tool. The results show that our model accurately predicts the coupling factor and its results can be safely assumed for the latter stages of the system and circuit design.

Table 5.2 presents the DC to RF conversion efficiency of the transmitter block over process corners, for input DC power around 100 mW. For these simulations, the transmitter is completely isolated from the receiver ($k = 0$). We see that the best efficiency occurs at the slow corner, suggesting that a higher

[1] In healthy adults, body temperature is about 37 ± 0.5 °C [88].
[2] Inductance and Capacitance Calculations by Decomposition in Thin Rings.

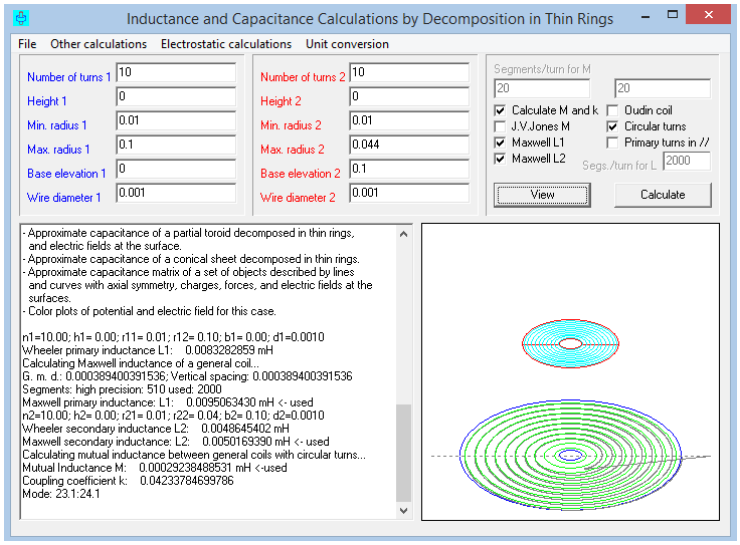

Figure 5.1: Screenshot of the ICCDTR tool.

Table 5.1: Comparison of the coupling factor model with the ICCDTR tool.

Distance ratio	**Size ratio**				
	1	2	3	4	5
1	$\frac{0.124}{0.118}$	$\frac{0.111}{0.107}$	$\frac{0.072}{0.0685}$	$\frac{0.047}{0.046}$	$\frac{0.034}{0.033}$
2	$\frac{0.035}{0.034}$	$\frac{0.0518}{0.049}$	$\frac{0.0462}{0.045}$	$\frac{0.037}{0.035}$	$\frac{0.029}{0.0278}$
3	$\frac{0.0138}{0.0132}$	$\frac{0.025}{0.024}$	$\frac{0.028}{0.0269}$	$\frac{0.025}{0.025}$	$\frac{0.023}{0.021}$
4	$\frac{0.0065}{0.0062}$	$\frac{0.013}{0.0128}$	$\frac{0.017}{0.0165}$	$\frac{0.0179}{0.017}$	$\frac{0.062}{0.016}$
5	$\frac{0.0035}{0.0033}$	$\frac{0.0077}{0.0074}$	$\frac{0.011}{0.0104}$	$\frac{0.0123}{0.0118}$	$\frac{0.0125}{0.012}$

threshold voltage in the switch is beneficial to the performance of this block. This is indeed accurate, and is because at lower V_{th} the leakage current is higher than for higher V_{th}. Depending on the specific application, the usage of external power transistors may be recommended. These transistors possess higher voltage and power ratings (and higher V_{th}) but for the input power levels required here, the transistors offered in the technology performed better than the external and were thus selected.

Table 5.2: Transmitter DC to RF efficiency over corners.

Transmitter			
Corner	**DC Power [mW]**	**RF Power [mW]**	**Efficiency [%]**
Typical	100.8	92.9	92.16
Slow	99.6	101.2	98.4
Fast	101.7	77.2	75.91

Another interesting validation is the one regarding the generalized model. Using this model, we could estimate the efficiency of a link based on the system's quality factor and the coupling factor. In our case, only the resonance scenario is of relevance since our transmitter operates in this regime. For this analysis, the system's quality factor is set to 160 approximately by setting the appropriate parasitic values at both the transmitter and the receiver. Table 5.3 presents the values of the predicted efficiency, defined by Eqs. (2.21) and (2.20), the efficiency of the magnetic part only (without considering the DC to RF conversion losses) and the entire link efficiency (including DC to RF conversion losses) for 5 different coupling factor values within our design space (0.004 to 0.04).

Table 5.3: Comparison of the generalized model with the circuit simulations.

Coupling factor	**Efficiency [%]**		
	Model prediction	**Magnetic only**	**Complete link**
0.004	8.6	10.3	8.8
0.008	23.8	19.1	11.0
0.01	30.7	21.6	9.2
0.02	54.0	42.5	33.3
0.04	73.25	74.0	52.6

Results show that the model consistently overestimates the efficiency of the magnetic link in around 20 %, except for the case when $k = 0.04$, in which both values are almost equal. Although this is a significant error, the validity of the model still holds as an upper limit determinator for links in resonance.

Fig. 5.2 shows the the voltage at the output of the rectifier as a function of

the coupling factor. In this simulation the rectifier is loaded only with the smoothing capacitor in order to determine the range of voltages that could be induced. We observe that for the coupling factors studied the output voltage of the unloaded rectifier ranges between 1.3 and 1.7 V.

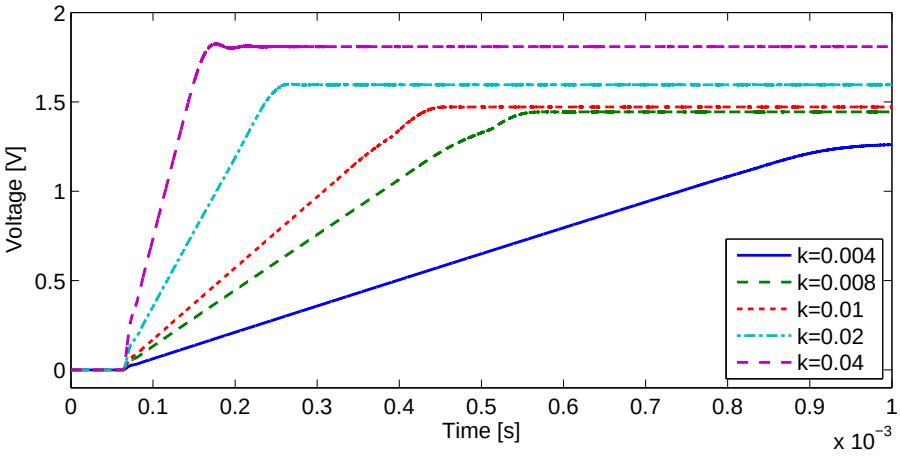

Figure 5.2: Rectifier voltage at different coupling factors.

If we were to emulate a Li-Ion battery, we would need to connect a huge capacitor in the output node. For instance, a battery with a capacity of 100 mAh (one of the smallest available for this kind of applications) corresponds to an equivalent charge of 360 Coulombs. At 4.2 V, this represents an equivalent capacitance of 85.7 F approximately, an intractable value for simulations. For validation and simulation speed, we use smaller capacitors. Here, the choice is made based on the allowable ripple at the output node. Thus, a 1 μF capacitor is used as the battery when analyzing the boost converter and the entire system.

Fig. 5.3 shows the charging process in the boost converter fed by the rectifier only (the transmitter is left aside for simulation speed). Fig. 5.3(a) resembles very much the results from the *Simulink* model presented in Fig. 4.17. Fig. 5.3(b) shows the transistion between the Boundary Regulated Mode and the Voltage Regulated Mode. As we discussed in the design chapter, the switching frequency of the boost converter adapts itself during the charging process depending on the output voltage. In our design, the switching frequency of the boost converter ranges from 98kHz (depleted battery) to 108kHz (full battery).

Fig. 5.4 presents the efficiency of the boost converter (only) as a function of the input power. The circuit achieves a peak efficiency η_{peak} of 81.8 % at 4 mW input and is able to operate down to input powers of -16.2 dBm. We can

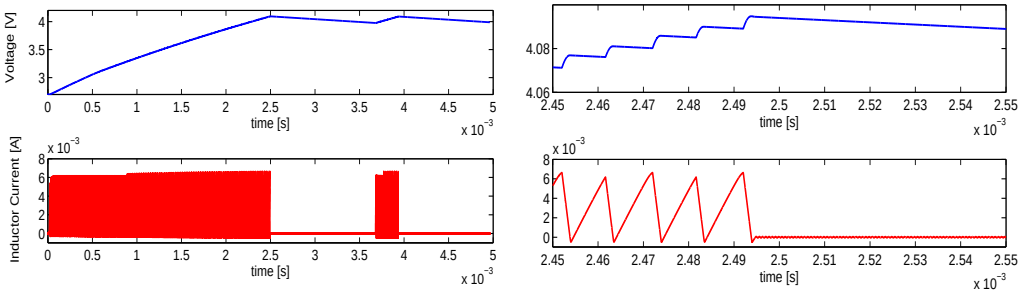

(a) Charging profile.

(b) Zoom in the transistion between BRM and VRM.

Figure 5.3: Boost converter output voltage and inductor current.

observe a somewhat flat efficiency curve in the range of 500 μW to 10 mW. Under 500 μW, the efficiency drops rather quickly. We know that at low input powers, switching is the major source of losses. Therefore, one could further improve the efficiency of the converter by adapting the size of the switches to the power available. The minimum input voltage for the digital circuitry to operate correctly is found to be around 0.92 V for the typical corner. Hence, considering Fig. 5.2 we can state that the circuit could still extract power from the transmitter for distances larger than 10 cm (corresponding to $k = 0.004$) or larger misalignments. Under this voltage, the delay in the digital cells is too large and the control fails to give a regulated output. Considering this is a 1.8 V technology, the minimum operating voltage we obtained here is quite acceptable.

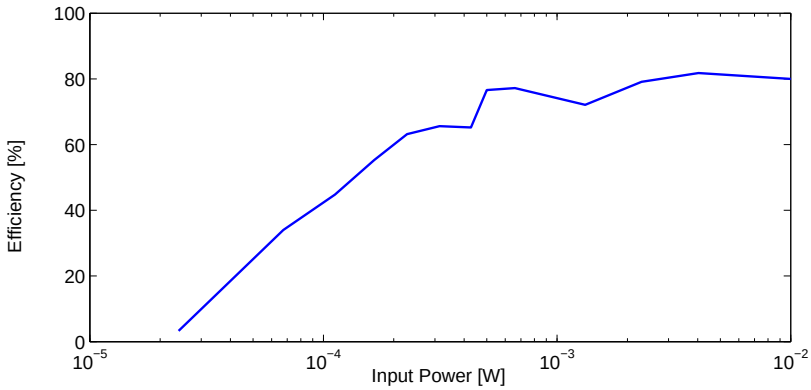

Figure 5.4: Efficiency of the boost converter vs. input power.

We also analyze the impact of process variations in the regulated output voltage via corner analysis. Five corners are considered for this analysis. Table 5.4 presents the results obtained.

Table 5.4: Regulated output voltage.

	Corner				
Voltage [V]	**TT**	**SS**	**FF**	**SF**	**FS**
	4.13	4.09	4.12	4.07	4.1

Table 5.5 summarizes the most important specifications of the designed boost converter.

Table 5.5: Boost converter specifications

Specification	**Value**
V_{out}	4.1 [V] $\pm$ 30 [mV]
η_{peak}	81.8 [%]
$P_{IN_{min}}$	-16.2 [dBm]
f_{switch}	98–108 [kHz]

Finally, Figs. 5.5 and 5.6 illustrates the charging process of the entire WPT system for different coupling factors. Naturally, for lower coupling, the circuit takes longer to charger due to the less available power. In all cases, however, the system properly regulates the voltage at the intended value.

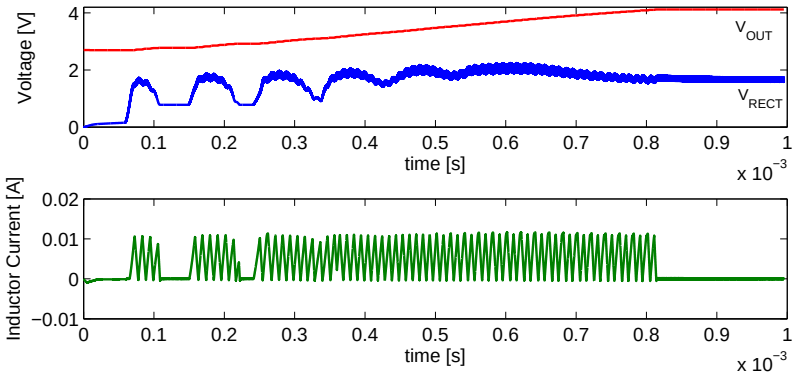

Figure 5.5: Charging profile for $k = 0.04$.

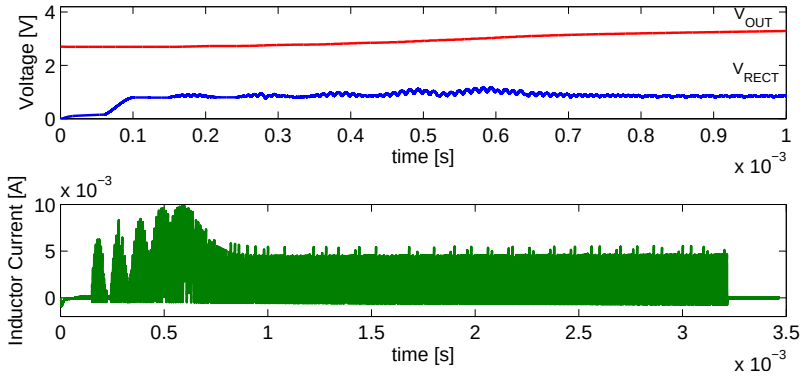

Figure 5.6: Charging profile for $k = 0.004$.

Chapter 6

Conclusions and Recommendations

In this chapter, the keypoints of the previously discussed topics are brought together in the conclusions section. This is then followed by a section in which we present an overview of the scientific contributions made in this work. Lastly, a set of recommendations is given for future work in this area.

6.1 Conclusions

In this work, the general idea of transferring energy wirelessly to an implantable device is addressed. Several techniques were analyzed from literature, but finally near field inductive coupling was selected due its flexibility in terms of power and size and the maturity when compared to the rest. The models developed in Ch. 2 showed that coupling factors of less than 0.04 should be expected, effectively imposing a weakly coupled regime.

The results of our model match to a great extent with those available in specific tools for the calculation of coupling factors of coils. From here, an efficiency analysis was made by means of a generalized model. Larger Tx/Rx ratios would have a smaller peak efficiency but more uniform with distance and

misalignment changes. If the application in question has a fixed distance and/or area, one can determine a coil configuration for optimal performance. Since in our case we account for variable positions, coil misalignments had to be addressed. Our findings indicate that the impact of both angular and lateral misalignment only play a significant role if the distance between the coils is very small.

Resonance arises as an important tool to overcome some of the drawbacks of operating with weakly coupling factors. From our models we could observe that at least a 10x improvement in the loss factor could be achieved when using resonance over the non-resonant counterpart.

By analyzing tissue characteristics over frequency in conjunction with current regulations and the specific absorption rate due to both electric and magnetic field, we could establish a relation between them and observe that for the relevant tissues (and in general for any biological tissue), near field inductive coupling offers less tissue absorption than its far field counterpart.

From here, the design of a near field WPT system was undertaken. The power transmitter shows a DC to RF conversion efficiency of 92 % at 100 mW input for the typical corner and a worst case efficiency of 76 %. This results are in line with the efficiency values reported in literature.

The rectifier and boost converter have to be design together to be able to reach good performance. The load of the rectifier and the input voltage determine to a great extent the efficiency of the full-wave cross-coupled rectifier. The usage of the inductor voltage as a control signal allows us to avoid any extra resistance in the current path for zero-crossing detection. However, we must be aware that this is only possible because the reverse current flow charges back the smoothing capacitor of the rectifier, effectively storing the energy for its usage in the next charging cycle. The price to pay is some extra conduction losses due to the continuous back and forth flow of this current.

Simulation results show that the low power boost converter has a peak efficiency of 81.8 % and over 50 % efficiency for a two decade input power span, from -10 to 10 dBm. Moreover, it is able to operate at input powers as low as -16.2 dBm. The output voltage regulation is tested across corners showing good accuracy.

6.2 Contributions

- ***A model for the coupling factor of coils combining distance, size ratio and misalignment is developed***
  We developed a model that allows us to estimate the coupling factor of circular spiral coils in space. Using the receiver radius as a reference quantity allows us to extract valuable information and draw conclusions from the model regardless of effective dimensions of the coils.

- ***A generalized model of the inductive link is developed***
  We created a model that allows us to estimate the system's performance in terms of power efficiency and determine certain design pathways taking into account device characteristics (such as Q) and spatial conditions (such as k). This model serves as a valid starting point in defining the maximal achievable efficiency. Circuit simulation show consistency between the predicted performance and the actual performance at transistor level.

- ***A study of the effects of WPT in tissue is presented***
  Studying how tissue reacts to near field WPT is as important as to know how tissue affects the performance of the link. E-field induced SAR has been treated extensively in literature, but this is not the case for H-field. Using the current regulations of magnetic field exposure, tissue characteristics and fundamental electromagnetics we present a study of the specific absorption rate involving both electric and magnetic fields.

- ***An entire near field WPT system is designed***
  Combining the lessons learned during this work with our background knowledge, a complete near field WPT system is designed at a circuit level. This includes a resonant power transfer interface, a rectifying stage and a 4.15 V boost converter with an asynchronous digital control. The circuits are verified for conventional operating point as well as corners.

6.3 Recommendations

- *Modeling*
  The models that were developed proved to be of great help in the understanding of the near field WPT and in the decision making while the design task was undertaken. Still, other geometries such as the solenoid and circular and square spiral could be introduced. This would allow us not only to determine their individual characteristics, but also to compare them and determine the best option for a particular situation. Moreover, extending the validity of the model for larger lateral misalignments would further enhance our understanding of the link and allow us to evaluate (or re-evaluate) the applicability of the near field WPT in other applications.

- *Circuit design*
  Some of the decisions made throughout the design of the system were "second best" choices, mainly due to time constraints and complexities implementing the best solution. Following this line, a better digital control could be achieved if the programmable delay approach is implemented. Of course, beforehand is hard to judge how beneficial this can be in terms of power efficiency. Synthesizing the digital circuitry using hardware definition languages could come in handy but, if the selected operating voltages are outside the range defined for by the foundry for standard cells, they may fail to perform properly thus making necessary a full-custom digital design.

  In our design, all the digital circuitry is connected to the output of the rectifier. It is done this way because at the beginning it is assumed there is no energy available at the output node (or if there is, is not supposed to drive the boost converter). This provides us with relatively small driving voltages for the boost converter switches. If, however, the buffers driving the switches could be connected to the output node once the circuit has started up and there is enough energy available, the R_{ON} of the switches would drastically reduce, improving overall system performance. To achieve this, a system that intelligently toggles the voltage source of the buffers from one place to another is necessary.

  Although the design has been verified by means of corners analysis, this does not include any parasitics that may appear after the real silicon implementation. Therefore, the *Layout* design of the circuit should be undertaken to be the closest to reality possible. Furthermore, manufacturing and measuring should be the ultimate target towards the complete validation of the design methodology and results presented in this work.

Appendix A

Matlab scripts

A.1 Implemented codes

A.1.1 Radiation Resistance of Coils

```
% This script calculates the radiation resistance based on the method
% presented by Balanis. The calculations are made for free space.

% The radiation resistance is given by the following expression
% Rrad = 20*pi^2*N^2*(l/lambda)^4 [Ohms]

f=logspace(6,9,60);
c=1e8; %speed of light in free space
lambda=c./f;

% The following loops are assumed to have 1 cm radius.

circ = 2*pi*(0.01); % circumference of a single loop
N = [1 10]; % number of loops
l = circ.*N; % wire length vector
```

```
% radiation resistance calculation

for i=1:length(N)
    Rrad(i,:)=20*pi^2*N(i)^2.*(l(i)./lambda).^4;
end
```

A.1.2 Mutual inductance and Effect of Misalignment

```
clear all, close all
% This script calculates the mutual inductance as a function of the
coil
% radius, distance and number of turns of both transmitter and receiver.
% There are two methods presented, one from the book "Wireless Power
% Transfer" and the other from the article "Mutual Inductance and
% Inductance Calculation by Maxwell Method".

%% PARAMETERS
mu0 = 4*pi*1e-7; % Permeability of free space

a = 0.012; % fixed receiver radius in meters
na = 1; % fixed receiver number of turns
ha = 0.01; % height of the receiver in meters (only if na > 1)
ta = 0.5e-3; % thickness of the wire in meters (radius)

b = linspace(a/5,5*a,100); % transmitter radius in meters
nb = linspace(1,10,10); % transmitter number of turns
hb = 0.01; % height of the transmitter in meters (only if nb > 1)
tb = 0.5e-3; % thickness of the wire in meters (radius)

d = linspace(a/5,5*a,100); % Distance between the coils in meters
Q = 100; % Quality factor of the system

%% PART I: Inductance, mutual inductance and coupling factor
% CALCULATION OF INDIVIDUAL INDUCTANCES OF L1 AND L2

ka=4*a*(a-ta)/(2*a-ta)^2;
[K1,E1]=ellipke(ka);
L1=mu0*(2*a-ta)*((1-ka/2)*K1-E1);
```

```
kb(1,:)=4.*b.*(b-tb)./(2.*b-tb).^2;
[K2,E2]=ellipke(kb);
L2=mu0*(2.*b-tb).*((1-kb./2).*K2-E2);

%% MODULUS OF THE ELLIPTIC INTEGRALS (this is not the coupling factor
!)
% This parameter is given by the following expression:

%         2sqrt(ab)
% k = ------------------
%     sqrt((a+b)^2+d^2)

% Therefore, a vector of k must be generated as a function of the input
% parameters. This will be later used for the calculation of the mutual
% inductance using the elliptic integrals. Similarly, the coupling
% coefficient kfactor can be calculated as M12/sqrt(L1L2).

% The following approach was taken from the book "Wireless Power Transfer"
% ch. 5 "Magnetic Resonant Wireless Power Transfer" and for a single
loop
% is congruent with the results obtained using the INCA software based
on
% the Maxwell's method. INCA was developed by Prof. Queiroz from UFRJ.

x1=zeros(length(d),length(b));
x2=zeros(length(d),length(b));
km=zeros(length(d),length(b));
ksoma=zeros(length(d),length(b));

for i=1:length(d)
    x1(i,:)=(a^2+b.^2+d(i)^2)./(a^2.*b.^2);
    x2(i,:)=2/a./b;
    km(i,:)=2.*x2(i,:)./(x1(i,:)+(x2(i,:)));
end

[Km,Em]=ellipke(km);

%% MUTUAL INDUCTANCE AND COUPLING FACTOR CALCULATION
% Here it is required to compute the elliptic integrals of the first
and
% second kind as part of the mutual inductance calculation. Once the
both
% the individual and mutual inductances have been estimated it is possible
% to estimate the coupling factor as:
```

```
%              M12
% kfactor = ---------
%           sqrt(L1L2)

M12=zeros(length(d),length(b));
kfactor=zeros(length(d),length(b));
lossfactor=zeros(length(d),length(b));
eff=zeros(length(d),length(b));

for i=1:length(d)
    M12(i,:) = 2*mu0.*sqrt(x1(i,:)+x2(i,:))./x2(i,:) .*((1-km(i,:)/2)
.*Km(i,:)-Em(i,:));
    kfactor(i,:) = M12(i,:)./(sqrt(L1.*L2(1,:)));
    lossfactor(i,:)=2./(kfactor(i,:).*Q).^2 .* (1 + sqrt(1 + kfactor(i,:)
.*Q).^2);
    eff(i,:)=1./(1+lossfactor(i,:));
end

% Plot coupling factor vs. mutual inductance
v=zeros(1,4);
param=[0.5 1 2 5];
for i=1:length(v)
    for j=1:length(d)
    if d(j) >= param(i)*a;
        v(i) = j;
        break
    end
    end
end

%% PART II: Mutual inductance variation as a function of lateral and
angular misalignments
% Here we will study the variation of the mutual inductance (and coupling
% factor) as a function of lateral and angular misalignment, factors
that
% will play a significant role in the biomedical inductive link. We
will
% restrict the lateral misalignment up to a diameter of the receiver
coil
% and the angular misalignment up to 60 degrees. The radius of the
coils as
% well as the distance are fixed for each run.
```

```
clear km Km Em x1 x2

d = logspace(log10(a/10),log10(10*a),20);
b = a;
delta=linspace(eps,1*a,20);
angle=linspace(0,90-eps,20);

%% LATERAL MISALIGNMENT

% calculation of self inductances

ka=4*a*(a-ta)/(2*a-ta)^2;
[K1,E1]=ellipke(ka);
L1=mu0*(2*a-ta)*((1-ka/2)*K1-E1);

kb=4.*b.*(b-tb)./(2.*b-tb).^2;
[K2,E2]=ellipke(kb);
L2=mu0*(2.*b-tb).*((1-kb./2).*K2-E2);

% For a fixed distance, calculate the mutual inductance and coupling
factor
% as a function of the lateral misalignment.

km=zeros(length(d),length(delta));
x1=zeros(length(d),length(delta));
x2=zeros(length(d),length(delta));

for i=1:length(d)
    x1(i,:)=(a^2+(b-delta).^2+d(i)^2) ./(a^2.*(b-delta).^2);
    x2(i,:)=2/a./(b-delta);
    km(i,:)=2.*x2(i)./(x1(i)+(x2(i)));
end

[Km,Em]=ellipke(km);

M12=zeros(length(d),length(delta));
kfactor=zeros(length(d),length(delta));

for i=1:length(d)
    M12(i,:) = 2*mu0.*sqrt(x1(i,:)+x2(i,:)) ./x2(i,:).*((1-km(i,:)/2)
.*Km(i,:)-Em(i,:));
    kfactor(i,:) = abs(M12(i,:) ./(sqrt(L1.*L2(1,:))));
end
```

```
%% ANGULAR MISALIGNMENT

clear km Km Em x1 x2

% For a fixed distance, calculate the mutual inductance and coupling
factor
% as a function of the angular misalignment.

km=zeros(length(d),length(angle));
x1=zeros(length(d),length(angle));
x2=zeros(length(d),length(angle));

for i=1:length(d)
    x1(i,:)=(a^2+(b.*cosd(angle)) .^2+d(i)^2) ./(a^2.*(b.*cosd(angle)).^2);
    x2(i,:)=2/a./(b.*cosd(angle));
    km(i,:)=2.*x2(i)./(x1(i)+(x2(i)));
end

[Km,Em]=ellipke(km);

M12=zeros(length(d),length(angle));
kfactor=zeros(length(d),length(angle));

for i=1:length(d)
    M12(i,:) = 2*mu0.*sqrt(x1(i,:)+x2(i,:)) ./x2(i,:) .*((1-km(i,:)/2)
.*Km(i,:)-Em(i,:));
    kfactor(i,:) = M12(i,:) ./(sqrt(L1.*L2(1,:)));
end
```

A.1.3 Generalized model of the Inductive Link

```
%% LOSS FACTOR vs. MATCHING FACTOR
close all
QRx = [100 1000 40 300];
QTx = [100 1000 300 40];
Q = sqrt(QRx.*QTx);
q = sqrt(QRx./QTx);
X = [1 0];
gamma = logspace(-3,1,1000);
k = [1e-2 5e-2 1e-1 1 5e-1];
```

```
% PART I: OPTIMAL RESONANT MATCHING WITH EQUAL QUALITY FACTORS

lambdaRx = zeros(length(k),length(gamma));
lambdaTx = zeros(length(k),length(gamma));
lambda = zeros(length(k),length(gamma));

for i=1:length(k)
    lambdaRx(i,:) = 1./(q(1)*Q(1).*gamma);
    lambdaTx(i,:) = q(1)./(k(i)^2.*Q(1).*gamma) .* ( (gamma+ 1./(q(1)*Q(1))
).^2 + (1-X(1)).^2 );
    lambda(i,:) = lambdaRx(i,:)+lambdaTx(i,:);
end

var1=num2str(k(1)); var2=num2str(k(2)); var3=num2str(k(3)); var4=num2str(k(4));
str1 = ['k = ' var1];str2 = ['k = ' var2];str3 = ['k = ' var3];str4
= ['k = ' var4];

% PART II: RESONANT AND NON-RESONANT OPERATION FOR DIFFERENT k FACTORS
AND
% QUALITY FACTORS (THE QUALITY FACTORS COMPENSATING THE DROP IN k)

clear lambdaRx lambdaTx lambda

% low k high quality factor

lambdaRx(1,:) = 1./(q(1)*Q(1).*gamma);
lambdaTx(1,:) = q(1)./(k(2)^2.*Q(1).*gamma) .* ( (gamma+ 1./(q(1)*Q(1)))
.^2 + (1-X(1)).^2 );
lambda(1,:) = lambdaRx(1,:)+lambdaTx(1,:);
lambdaRx(2,:) = 1./(q(1)*Q(1).*gamma);
lambdaTx(2,:) = q(1)./(k(2)^2.*Q(1).*gamma) .* ( (gamma+ 1./(q(1)*Q(1)))
.^2 + (1-X(2)).^2 );
lambda(2,:) = lambdaRx(2,:)+lambdaTx(2,:);

var1=num2str(Q(2));
var2=num2str(k(2));
str1=['System Q = ' var1 ' and k = ' var2];

% high k low quality factor

lambdaRx(3,:) = 1./(q(2)*Q(2).*gamma);
lambdaTx(3,:) = q(2)./(k(5)^2.*Q(2).*gamma) .* ( (gamma+ 1./(q(2)*Q(2)))
.^2 + (1-X(1)).^2 );
```

```
lambda(3,:) = lambdaRx(3,:)+lambdaTx(3,:);
lambdaRx(4,:) = 1./(q(2)*Q(2).*gamma);
lambdaTx(4,:) = q(2)./(k(5)^2.*Q(2).*gamma) .* ( (gamma+ 1./(q(2)*Q(2)))
.^2 + (1-X(2)).^2 );
lambda(4,:) = lambdaRx(4,:)+lambdaTx(4,:);

var1=num2str(Q(1));
var2=num2str(k(5));
str1=['System Q = ' var1 ' and k = ' var2];
% PART III: RESONANT AND NON-RESONANT COUPLING WITH DIFFERENT QUALITY
% FACTORS FOR THE TRANSMITTER AND THE RECEIVER (TWO CASES)

clear lambdaRx lambdaTx lambda

% high quality of transmitter, poor receiver

lambdaRx(1,:) = 1./(q(3)*Q(3).*gamma);
lambdaTx(1,:) = q(3)./(k(3)^2.*Q(3).*gamma) .* ( (gamma+ 1./(q(3)*Q(3)))
.^2 + (1-X(1)).^2 );
lambda(1,:) = lambdaRx(1,:)+lambdaTx(1,:);
lambdaRx(2,:) = 1./(q(3)*Q(3).*gamma);
lambdaTx(2,:) = q(3)./(k(3)^2.*Q(3).*gamma) .* ( (gamma+ 1./(q(3)*Q(3)))
.^2 + (1-X(2)).^2 );
lambda(2,:) = lambdaRx(2,:)+lambdaTx(2,:);

var1=num2str(QRx(3));
var2=num2str(QTx(3));
var3=num2str(k(3));
str1=['QRx = ' var1 '; QTx = ' var2 '; k = ' var3];

% high quality of receiver, poor transmitter

clear lambdaRx lambdaTx lambda

lambdaRx(1,:) = 1./(q(4)*Q(4).*gamma);
lambdaTx(1,:) = q(4)./(k(3)^2.*Q(4).*gamma) .* ( (gamma+ 1./(q(4)*Q(4)))
.^2 + (1-X(1)).^2 );
lambda(1,:) = lambdaRx(1,:)+lambdaTx(1,:);
lambdaRx(2,:) = 1./(q(4)*Q(4).*gamma);
lambdaTx(2,:) = q(4)./(k(3)^2.*Q(4).*gamma) .* ( (gamma+ 1./(q(4)*Q(4)))
.^2 + (1-X(2)).^2 );
lambda(2,:) = lambdaRx(2,:)+lambdaTx(2,:);

var1=num2str(QRx(4));
```

```
var2=num2str(QTx(4));
var3=num2str(k(3));
str1=['QRx = ' var1 '; QTx = ' var2 '; k = ' var3];

% PART IV: FoM
% Here the figure of merit of the link, defined as kQ is plotted vs
the
% optimal loss factor.

kQ=logspace(-1,3,1000);
lopt = 2./(kQ).^2.*(1+sqrt(1+(kQ).^2));
```

Bibliography

[1] M. R. Yuce, "Implementation of wireless body area networks for healthcare systems," *Sensors and Actuators A: Physical*, vol. 162, no. 1, pp. 116–129, 2010.

[2] A. B. Intelligence, "Wearable sports and fitness devices will hit 90 million shipments in 2017," Feb. 2012. http://www.abiresearch.com/press/wearable-_sports-_and-_fitness-_devices-_will-_hit-_90-_mi.

[3] L. Brookes, "Discussing healthcare: Where will we be in 2050," *Medical solutions. Siemens healthcare magazine*, May 2010.

[4] J. Paulo and P. Gaspar, "Review and future trend of energy harvesting methods for portable medical devices," in *Proceedings of the World Congress on Engineering*, vol. 2, 2010.

[5] J. Paradiso and T. Starner, "Energy scavenging for mobile and wireless electronics," *Pervasive Computing, IEEE*, vol. 4, no. 1, pp. 18–27, 2005.

[6] M. Zeman, *Introduction to photovoltaic solar energy*. TU-Delft, 2011.

[7] R. Vullers, R. van Schaijk, I. Doms, C. Van Hoof, and R. Mertens, "Micropower energy harvesting," *Solid-State Electronics*, vol. 53, no. 7, pp. 684–693, 2009.

[8] P. Mitcheson, E. Yeatman, G. Rao, A. Holmes, and T. Green, "Energy harvesting from human and machine motion for wireless electronic devices," *Proceedings of the IEEE*, vol. 96, no. 9, pp. 1457–1486, 2008.

[9] S. Ayazian and A. Hassibi, "Delivering optical power to subcutaneous implanted devices," in *Engineering in Medicine and Biology Society, EMBC, 2011 Annual International Conference of the IEEE*, pp. 2874–2877, IEEE, 2011.

[10] K. R. Byrnes, R. W. Waynant, I. K. Ilev, X. Wu, L. Barna, K. Smith, R. Heckert, H. Gerst, and J. J. Anders, "Light promotes regeneration and functional recovery and alters the immune response after spinal cord injury," *Lasers in Surgery and Medicine*, vol. 36, no. 3, pp. 171–185, 2005.

[11] K. Goto, T. Nakagawa, O. Nakamura, and S. Kawata, "An implantable power supply with an optically rechargeable lithium battery," *Biomedical Engineering, IEEE Transactions on*, vol. 48, no. 7, pp. 830–833, 2001.

[12] T. Oshita and R. Calderhead, *Low Level Laser Therapy: A practical Introduction*. Wiley, 1988.

[13] J. Olivo, S. Carrara, and G. De Micheli, "Energy harvesting and remote powering for implantable biosensors," *Sensors Journal, IEEE*, vol. 11, no. 7, pp. 1573–1586, 2011.

[14] J. Stevens, "Optimized thermal design of small δt thermoelectric generators," in *Proc. 34th Intersociety Energy Conversion Engineering Conference, paper*, pp. 01–2564, 1999.

[15] V. Leonov, T. Torfs, P. Fiorini, and C. Van Hoof, "Thermoelectric converters of human warmth for self-powered wireless sensor nodes," *Sensors Journal, IEEE*, vol. 7, no. 5, pp. 650–657, 2007.

[16] P. Wright, "Energy harvesting in the human body (implantable self-powered sensors)," June 2008.

[17] M. Strasser, R. Aigner, C. Lauterbach, T. Sturm, M. Franosch, and G. Wachutka, "Micromachined cmos thermoelectric generators as on-chip power supply," *Sensors and Actuators A: Physical*, vol. 114, no. 2, pp. 362–370, 2004.

[18] T. energy Corporation., "Thermolife characteristics," 2008. http://www.poweredbythermolife.com/thermolife.htm.

[19] P. Org, "Backpack straps harvest energy to power electronics," Sept. 2007. http://phys.org/news108897656.html.

[20] I. Spectrum, "Squishy power generators," Dec. 2012. http://spectrum.ieee.org/green-_tech/fuel-_cells/squishy-_power-_generators.

[21] M. Hayakawa, "A study of the new energy systems for quartz watches (ii) - the effective circuit for the system," *Congres europeen de chronometrie*, 1988.

[22] H. Goto, T. Sugiura, and T. Kazui, "Feasibility of the automatic generating system (ags) for quartz watches as a leadless pacemaker power source: a preliminary report," in *Engineering in Medicine and Biology Society, 1998. Proceedings of the 20th Annual International Conference of the IEEE*, pp. 417–419, IEEE, 1999.

[23] P. Miao, P. Mitcheson, A. Holmes, E. Yeatman, T. Green, and B. Stark, "Mems inertial power generators for biomedical applications," *Microsystem Technologies*, vol. 12, no. 10, pp. 1079–1083, 2006.

[24] R. Tashiro, N. Kabei, K. Katayama, Y. Ishizuka, F. Tsuboi, and K. Tsuchiya, "Development of an electrostatic generator that harnesses the motion of a living body:(use of a resonant phenomenon)," *JSME international journal. Series C, Mechanical systems, machine elements and manufacturing*, vol. 43, no. 4, pp. 916–922, 2000.

[25] R. Elfrink, T. Kamel, M. Goedbloed, S. Matova, D. Hohlfeld, Y. Van Andel, and R. Van Schaijk, "Vibration energy harvesting with aluminum nitride-based piezoelectric devices," *Journal of Micromechanics and Microengineering*, vol. 19, no. 9, p. 094005, 2009.

[26] M. Renaud, K. Karakaya, T. Sterken, P. Fiorini, C. Van Hoof, and R. Puers, "Fabrication, modelling and characterization of mems piezoelectric vibration harvesters," *Sensors and Actuators A: Physical*, vol. 145, pp. 380–386, 2008.

[27] M. H. Nehrir and C. Wang, *Modeling and control of fuel cells: distributed generation applications*, vol. 41. Wiley-IEEE Press, 2009.

[28] J. Larminie and A. Dicks, "Fuel cells explained," 2000.

[29] R. A. Bullen, T. Arnot, J. Lakeman, and F. Walsh, "Biofuel cells and their development," *Biosensors and Bioelectronics*, vol. 21, no. 11, pp. 2015–2045, 2006.

[30] California Stationary Fuel Cell Collaborative, "Fuel cell technologies," July 2010.

[31] P. Malachesky, G. Holleck, F. McGovern, and R. Devarakonda, "Parametric studies of implantable fuel cell," in *Proceedings of the 7th Intersociety Energy Conversion Engineering Conference*, pp. 727–732, 1972.

[32] R. Drake, B. Kusserow, S. Messinger, and S. Matsuda, "A tissue implantable fuel cell power supply," *ASAIO Journal*, vol. 16, no. 1, pp. 199–205, 1970.

[33] N. Mano, F. Mao, A. Heller, *et al.*, "Characteristics of a miniature compartment-less glucose-o2 biofuel cell and its operation in a living plant," *Journal of the American Chemical Society*, vol. 125, no. 21, pp. 6588–6594, 2003.

[34] M. Stoopman, "UWB RFID tag scenario comparison," March 2011.

[35] H. J. Visser, A. C. Reniers, and J. A. Theeuwes, "Ambient RF energy scavenging: Gsm and wlan power density measurements," in *Microwave Conference, 2008. EuMC 2008. 38th European*, pp. 721–724, IEEE, 2008.

[36] D. Bouchouicha, F. Dupont, M. Latrach, and L. Ventura, "Ambient RF energy harvesting," in *IEEE Int. Conf. Renewable Energies Power Quality (ICREPQ'10)*, pp. 486–495, 2010.

[37] H. Le, N. Fong, and H. C. Luong, "RF energy harvesting circuit with on-chip antenna for biomedical applications," in *Communications and Electronics (ICCE), 2010 Third International Conference on*, pp. 115–117, IEEE, 2010.

[38] C. M. JOHN, V. JOHN, and M. H. MICKLE, "Device for brain stimulation using RF energy harvesting," March 2006. WO Patent WO/2006/029,007.

[39] R. Sarpeshkar, *Ultra low power bioelectronics*, vol. 1. Cambridge University Press Cambridge, UK, 2010.

[40] K. Kalyanasundaram and M. Graetzel, "Artificial photosynthesis: biomimetic approaches to solar energy conversion and storage," *Current opinion in Biotechnology*, vol. 21, no. 3, pp. 298–310, 2010.

[41] I. McConnell, G. Li, and G. W. Brudvig, "Energy conversion in natural and artificial photosynthesis," *Chemistry & biology*, vol. 17, no. 5, pp. 434–447, 2010.

[42] M. Katterle, V. I. Prokhorenko, A. R. Holzwarth, and A. Jesorka, "An artificial supramolecular photosynthetic unit," *Chemical Physics Letters*, vol. 447, no. 4, pp. 284–288, 2007.

[43] M. Grätzel, "Photoelectrochemical cells," *Nature*, vol. 414, no. 6861, pp. 338–344, 2001.

[44] M. Kline, I. Izyumin, B. Boser, and S. Sanders, "Capacitive power transfer for contactless charging," in *Applied Power Electronics Conference and Exposition (APEC), 2011 Twenty-Sixth Annual IEEE*, pp. 1398–1404, IEEE, 2011.

[45] S. Hui and W. W. Ho, "A new generation of universal contactless battery charging platform for portable consumer electronic equipment," *Power Electronics, IEEE Transactions on*, vol. 20, no. 3, pp. 620–627, 2005.

[46] M. Ghovanloo and K. Najafi, "A high data transfer rate frequency shift keying demodulator chip for the wireless biomedical implants," in *Circuits and Systems, 2002. MWSCAS-2002. The 2002 45th Midwest Symposium on*, vol. 3, pp. III–433, IEEE, 2002.

[47] A. Yakovlev, S. Kim, and A. Poon, "Implantable biomedical devices: wireless powering and communication," *Communications Magazine, IEEE*, vol. 50, no. 4, pp. 152–159, 2012.

[48] J. Sun and K. Hynynen, "Focusing of therapeutic ultrasound through a human skull: a numerical study," *The Journal of the Acoustical Society of America*, vol. 104, p. 1705, 1998.

[49] Wireless Power Consortium, "Cordless kitchen appliances: A powerful new kitchen concept," Apr. 2013. http://tinyurl.com/m73gzoe.

[50] W. U. in St. Louis, "Deep brain stimulation offers relief from symptomps of parkinson's disease," Feb. 2012. http://mpaweb1.wustl.edu/~medschool/outlookarchives/spring2002/parkinsons.html.

[51] K. Fotopoulou and B. Flynn, "Inductive wireless power transfer using circuit theory," *Wireless Power Transfer*, p. 109, 2012.

[52] J. D. Kraus, *Antennas*. {McGraw-Hill Education}, 1988.

[53] A. Umenei, "Understanding low frequency non-radiative power transfer," *Wireless Power Consortium contribution by Fulton Innovation LLC*, vol. 7575, 2011.

[54] J. I. Agbinya, *Wireless power transfer*. River Publishers, 2012.

[55] K. Finkenzeller and R. Waddington, *RFID Handbook: Radio-frequency identification fundamentals and applications*. Wiley New York, 1999.

[56] G. Wang, W. Liu, M. Sivaprakasam, and G. A. Kendir, "Design and analysis of an adaptive transcutaneous power telemetry for biomedical implants," *Circuits and Systems I: Regular Papers, IEEE Transactions on*, vol. 52, no. 10, pp. 2109–2117, 2005.

[57] M. Suster, D. J. Young, and W. H. Ko, "Micro-power wireless transmitter for high-temperature mems sensing and communication applications," in *Micro Electro Mechanical Systems, 2002. The Fifteenth IEEE International Conference on*, pp. 641–644, IEEE, 2002.

[58] D. C. Galbraith, M. Soma, and R. L. White, "A wide-band efficient inductive transdennal power and data link with coupling insensitive gain," *Biomedical Engineering, IEEE Transactions on*, no. 4, pp. 265–275, 1987.

[59] C. A. Balanis, *Antenna theory: analysis and design*. John Wiley & Sons, 2012.

[60] M. Soma, D. C. Galbraith, and R. L. White, "Radio-frequency coils in implantable devices: misalignment analysis and design procedure," *Biomedical Engineering, IEEE Transactions on*, no. 4, pp. 276–282, 1987.

[61] K. Fotopoulou and B. W. Flynn, "Wireless power transfer in loosely coupled links: Coil misalignment model," *Magnetics, IEEE Transactions on*, vol. 47, no. 2, pp. 416–430, 2011.

[62] M. Dionigi, A. Costanzo, F. Mastri, and M. Mongiardo, "Magnetic resonant wireless power transfer," *Wireless Power Transfer*, p. 159, 2012.

[63] A. C. M. de Queiroz, "Mutual inductance and inductance calculations by maxwell's method," *Home page of Dr. Antonio Carlos M. de Queiroz*, 2005.

[64] E. Waffenschmidt and T. Staring, "Limitation of inductive power transfer for consumer applications," in *Power Electronics and Applications, 2009. EPE'09. 13th European Conference on*, pp. 1–10, IEEE, 2009.

[65] E. Waffenschmidt, "Wireless power for mobile devices," in *Telecommunications Energy Conference (INTELEC), 2011 IEEE 33rd International*, pp. 1–9, IEEE, 2011.

[66] B. V. für Sicherheit and G. bei der Arbeit, "Elektromagnetische felder (bgv b11)(06.01)," *Carl Heymanns, Köln*, 2001.

[67] A. Ahlbom, U. Bergqvist, J. Bernhardt, J. Cesarini, M. Grandolfo, M. Hietanen, A. Mckinlay, M. Repacholi, D. Sliney, J. Stolwijk, *et al.*, "Guidelines for limiting exposure to time-varying electric, magnetic, and electromagnetic fields (up to 300 ghz). international commission on non-ionizing radiation protection.," *Health Phys*, vol. 74, no. 4, pp. 494–522, 1998.

[68] J. I. Agbinya, "Microwave propagation and inductive energy coupling in biological skin for body area network channels," *Wireless Power Transfer*, p. 339, 2012.

[69] J. B. Schneider, "Understanding the finite-difference time-domain method," *Scholl of electrical engineering and computer science Washington State University.– URL: http://www. eecs. wsu. edu/˜ schneidj/ufdtd/(request data: 29.11. 2012)*, 2010.

[70] A. K. Jonscher, "Dielectric relaxation in solids," *Journal of Physics D: Applied Physics*, vol. 32, no. 14, p. R57, 1999.

[71] C. Gabriel, "Compilation of the dielectric properties of body tissues at rf and microwave frequencies.," tech. rep., DTIC Document, 1996.

[72] A. Peyman, S. Holden, S. Watts, R. Perrott, and C. Gabriel, "Dielectric properties of porcine cerebrospinal tissues at microwave frequencies: in vivo, in vitro and systematic variation with age," *Physics in medicine and biology*, vol. 52, no. 8, p. 2229, 2007.

[73] D. Andreuccetti, R. Fossi, and C. Petrucci, "Calculation of the dielectric properties of body tissues," Feb. 2012. http://niremf.ifac.cnr.it/tissprop/htmlclie/htmlclie.htm.

[74] S. Gabriel, R. Lau, and C. Gabriel, "The dielectric properties of biological tissues: Iii. parametric models for the dielectric spectrum of tissues," *Physics in medicine and biology*, vol. 41, no. 11, p. 2271, 1996.

[75] A. I. Sabbah, N. I. Dib, and M. A. Al-Nimr, "Sar and temperature elevation in a multi-layered human head model due to an obliquely incident plane wave," *Progress In Electromagnetics Research M*, vol. 13, pp. 95–108, 2010.

[76] N. Kuster and Q. Balzano, "Energy absorption mechanism by biological bodies in the near field of dipole antennas above 300 mhz," *Vehicular Technology, IEEE Transactions on*, vol. 41, no. 1, pp. 17–23, 1992.

[77] D. M. Spillman and E. S. Takeuchi, "Lithium ion batteries for medical devices," in *Battery Conference on Applications and Advances, 1999. The Fourteenth Annual*, pp. 203–208, IEEE, 1999.

[78] S. Dearborn, "Charging li-ion batteries for maximum run times," *Power Electron. Technol. Mag*, vol. 31, no. 4, pp. 40–49, 2005.

[79] PowerStream, "Lithium-ion battery and lithium-iron-phosphate battery charging basics," Aug. 2013. http://www.powerstream.com/li.htm.

[80] S. Jeon, A. Suarez, and D. B. Rutledge, "Nonlinear design technique for high-power switching-mode oscillators," *Microwave Theory and Techniques, IEEE Transactions on*, vol. 54, no. 10, pp. 3630–3640, 2006.

[81] V. Rizzoli, A. Costanzo, F. Mastri, and C. Cecchetti, "Harmonic-balance optimization of microwave oscillators for electrical performance, steady-state stability, and near-carrier phase noise," in *Microwave Symposium Digest, 1994., IEEE MTT-S International*, pp. 1401–1404, IEEE, 1994.

[82] A. Costanzo, M. Dionigi, F. Mastri, and M. Mongiardo, "Rigorous modeling of mid-range wireless power transfer systems based on royer oscillators," in *Wireless Power Transfer (WPT), 2013 IEEE*, pp. 69–72, IEEE, 2013.

[83] S. Hashemi, M. Sawan, and Y. Savaria, "A high-efficiency low-voltage cmos rectifier for harvesting energy in implantable devices," *Biomedical Circuits and Systems, IEEE Transactions on*, vol. 6, no. 4, pp. 326–335, 2012.

[84] U. Karthaus and M. Fischer, "Fully integrated passive uhf rfid transponder ic with 16.7-μw minimum rf input power," *Solid-State Circuits, IEEE Journal of*, vol. 38, no. 10, pp. 1602–1608, 2003.

[85] P. Rakers, L. Connell, T. Collins, and D. Russell, "Secure contactless smartcard asic with dpa protection," *Solid-State Circuits, IEEE Journal of*, vol. 36, no. 3, pp. 559–565, 2001.

[86] R. W. Erickson and D. Maksimovic, *Fundamentals of power electronics*. Springer, 2001.

[87] C. Qiao and J. Zhang, "Control of boost type converter at discontinuous conduction mode by controlling the product of inductor voltage-second," in *Power Electronics Specialists Conference, 2005. PESC'05. IEEE 36th*, pp. 1213–1219, IEEE, 2005.

[88] Wikipedia, "Human body temperature," Aug. 2013. http://en.wikipedia.org/wiki/Human_body_temperature.